Mon. Not. R. Astron. Soc. **000**, 000–000 (0000) Printed 12 September 2014 (MN LATEX style file v2.2)

Cyclotron line signatures of thermal and magnetic mountains from accreting neutron stars

M. Priymak,[1⋆] A. Melatos,[1] & P. D. Lasky[1]
[1]*School of Physics, University of Melbourne, Parkville, VIC 3010, Australia*

12 September 2014

arXiv:1409.3327v1 [astro-ph.HE] 11 Sep 2014

ABSTRACT
Cyclotron resonance scattering features (CRSFs) in the X-ray spectrum of an accreting neutron star are modified differently by accretion mounds sustained by magnetic and thermocompositional gradients. It is shown that one can discriminate, in principle, between mounds of different physical origins by studying how the line energy, width, and depth of a CRSF depend on the orientation of the neutron star, accreted mass, surface temperature distribution, and equation of state. CRSF signatures including gravitational light bending are computed for both phase-resolved and phase-averaged spectra on the basis of self-consistent Grad-Shafranov mound equilibria satisfying a global flux-freezing constraint. The prospects of multimessenger X-ray and gravitational-wave observations with future instruments are canvassed briefly.

Key words: accretion, accretion disks – gravitational waves – stars: magnetic field – stars: neutron – pulsars: general

1 INTRODUCTION

Recent theoretical modeling has started to elucidate the structural differences between neutron star accretion mounds ('mountains') sustained by temperature gradients and elastic stresses on the one hand (Ushomirsky et al. 2000; Haskell et al. 2006) and magnetic stresses on the other (Brown & Bildsten 1998; Payne & Melatos 2004; Haskell et al. 2008; Priymak et al. 2011; Mukherjee & Bhattacharya 2012). In a thermal mountain, the temperature gradient at the base of the accreted crust creates kinetic pressure gradients and compositional (e.g. electron capture) gradients at the surface (Ushomirsky et al. 2000). The structure of the mountain and hence its permanent mass quadrupole moment are limited by the crustal breaking strain (Horowitz & Kadau 2009), the composition of the crust (Haskell et al. 2006), and whether or not the equation of state contains exotic species like hyperons or quarks (Nayyar & Owen 2006; Haskell et al. 2007; Johnson-McDaniel & Owen 2013). In a magnetic mountain, in contrast, the mountain structure and mass quadrupole are not limited by the crustal breaking strain. Magnetic stresses play the dominant role, and the detailed configuration of the surface magnetic field is mainly controlled by the total accreted mass, M_a (Priymak et al. 2011).

In this paper, we investigate how to use X-ray observations of cyclotron lines in accreting neutron stars to distinguish between mountains with different physical origins. The study is inspired by recent, pioneering calculations of the cyclotron resonance scattering features (CRSFs) produced by magnetized accretion mounds (Bhattacharya & Mukherjee 2011; Bhattacharya 2012; Mukherjee & Bhattacharya 2012; Mukherjee et al. 2013b,d,a,c).

It is important to find observational signatures to discriminate between thermal and magnetic mountains for two reasons. First, there remains considerable uncertainty regarding exactly how accreted material spreads away from the accretion column once it hits the stellar surface, and what this spreading does to the magnetic field. In high-mass X-ray binaries (HMXBs), for example, does a magnetic mountain form, with material confined at the pole by compressed equatorial magnetic field lines? Or does the accreted material cover the surface evenly, forming a thermal hot spot at the pole threaded by a dipolar magnetic field? Even in weakly magnetized systems like low-mass X-ray binaries (LMXBs), there exists evidence from the energies, recurrence times, and harmonic content of type I thermonuclear bursts that nuclear burning occurs in patches 'fenced off' by locally compressed magnetic fields much stronger than the global dipole field (Bhattacharyya & Strohmayer 2006; Payne & Melatos 2006; Misanovic et al. 2010; Cavecchi et al. 2011; Chakraborty & Bhattacharyya 2012). In strongly magnetized systems, like protomagnetars (Piro & Thrane 2012; Melatos & Priymak 2013) or young pulsars accreting from a fallback disk (Wang et al. 2006), the thermomagnetic structure of the accretion mound is completely unknown.

Second, the quadrupole moment of an accretion mound

⋆ E-mail: m.priymak@pgrad.unimelb.edu.au

is a gravitational wave source. In particular, LMXBs are a prime target of ground-based, long-baseline, gravitational-wave detectors like the Laser Interferometer Gravitational Wave Observatory (LIGO) and Virgo (Riles 2013), if they are in a state of torque balance, where the accretion torque equals the gravitational radiation reaction torque (Bildsten 1998; Watts et al. 2008)[1]. Of course, cyclotron lines have not yet been detected in LMXBs with millisecond periods, the strongest gravitational wave emitters. Common wisdom holds that this is not surprising because LMXBs are weakly magnetized, and it is true that their inferred magnetic dipole moments $\mu \sim 10^{26}$ G cm^3 are low. However, an alternative scenario is also possible: the cyclotron features are present as a result of the 'magnetic fences' discussed in the previous paragraph, but they are too weak to be detected by X-ray telescopes currently in operation. Recent rigourous theoretical calculations have provided support both to the idea of locally intense magnetic fields in low-μ objects (Payne & Melatos 2004, 2006; Vigelius & Melatos 2008; Priymak et al. 2011) and the idea that the resulting cyclotron lines are weak [see Mukherjee & Bhattacharya (2012) and also this paper], adding to the observational evidence from nuclear burning cited above [see also Patruno et al. (2012)]. If so, then interesting multimessenger (X-ray and gravitational wave) experiments become possible with future observatories.

CRSFs are X-ray absorption lines arising from resonant Compton scattering at quantised Landau energies in the presence of a strong magnetic field (Meszaros 1984; Harding 1991). They have been observed in several isolated neutron stars (Bignami et al. 2003; Haberl 2007) and 17 accreting X-ray pulsars to date (Makishima et al. 1999; Heindl et al. 2004; Caballero & Wilms 2012; Pottschmidt et al. 2012), as well as six unconfirmed candidates (Caballero & Wilms 2012; Pottschmidt et al. 2012). CRSFs allow an independent and direct measurement of surface magnetic field strengths between $\sim 10^{12}$ G and 10^{13} G. Several accreting pulsars display multiple, anharmonically-spaced CRSFs (Pottschmidt et al. 2012). This anharmonicity is more significant than expected from relativistic absorption effects (Harding & Lai 2006) and is attributed instead to local distortions of the magnetic field (Nishimura 2005), such as those predicted for magnetic mountains.

Numerous results have flowed from studies of CRSFs in accreting pulsars. Some systems such as Her X-1 (Staubert et al. 2007) and Vela X-1 (Fuerst et al. 2013) show a positive correlation between luminosity and cyclotron line energy, while others such as 4U 0115+63 (Mihara et al. 2004; Nakajima et al. 2006) and V 0332+53 (Tsygankov et al. 2010) show a negative correlation or none at all [e.g. A 0535+26 (Caballero et al. 2007)]. These trends are attributed to different accretion rates $\dot{M}$ (Basko & Sunyaev 1976; Nelson et al. 1993): at high $\dot{M}$, a radiation dominated shock forms in the accretion column, emitting a 'fan beam', whereas at low $\dot{M}$, a 'pencil beam' is emitted from near the surface. For fast accretors, the luminosity and line energy are anticorrelated because the magnetic field at the shock-front decreases with $\dot{M}$ (Burnard et al. 1991). CRSF line parameters such as depth, width, and central energy are also observed to vary with pulse phase in several sources (Kreykenbohm et al. 2004; Suchy et al. 2008, 2011). For example, Her X-1 displays a $\sim 25\%$ variation in line energy and $\sim 100\%$ variation in line width and depth over a single pulse (Klochkov et al. 2008). Phase-averaged spectra also exhibit relations between the line energy and the continuum break energy, line width and line energy, and fractional width and line depth (Heindl et al. 2004).

Mukherjee & Bhattacharya (2012) conducted a phase-resolved theoretical study of the effect of accretion-induced deformations of the local magnetic field on CRSFs, combining the results of Monte-Carlo simulations of photon propagation through magnetically threaded plasma (Araya & Harding 1999; Araya-Góchez & Harding 2000; Schönherr et al. 2007) with numerical solutions for the magnetohydrostatic structure of the accretion mound (Mouschovias 1974; Brown & Bildsten 1998; Litwin et al. 2001; Payne & Melatos 2004; Mukherjee et al. 2013b). They found that multiple anharmonic CRSFs are consistent with the distorted magnetic field produced by accretion-induced polar burial, with a strong dependence on the viewing geometry. They also found weak (strong) phase dependence in the case of symmetric (asymmetric) mounds at the two poles.

In this paper, we apply the above work to the following important practical question: can one use high-sensitivity X-ray spectra (and possibly simultaneous gravitational-wave data) to discriminate between a mountain of thermal and magnetic origin? We find that the answer is a qualified yes; in principle, the two sorts of mountain exhibit different instantaneous and phase-averaged CRSF line shapes, and different relations between the line shape and gravitational wave strain, which may be detectable statistically across the population even if not in individual objects. In the process, we generalize the work of Bhattacharya, Mukherjee, and Mignone (Mukherjee & Bhattacharya 2012; Mukherjee et al. 2013b,d) to include a systematic study of CRSF properties as functions of accreted mass, magnetic inclination, viewing angle, and equation of state. The paper is structured as follows. In Sections 2 and 3 we describe the numerical models used to generate magnetic mountains and cyclotron line spectra. We examine the effect of observer orientation and magnetic inclination angles on phase-resolved spectra in Section 4. We vary the accreted mass and surface temperature distribution in Section 5 and the equation of state in Section 6. Differences in spectral properties between magnetic and thermo-compositional mountains are discussed in Section 7, where we present a recipe for distinguishing in principle between a magnetic and thermal mountain, partly in preparation for the first searches for accreting neutron stars with Advanced LIGO and Virgo.

2 ACCRETION MOUND

We employ the analytical and numerical techniques discussed in detail in Priymak et al. (2011) to compute the equilibrium structure of a magnetized accretion mound, by

[1] Other physics may nullify the torque balance scenario, e.g. radiation pressure in the inner accretion disk (Andersson et al. 2005) or episodic cycles in the disk-magnetosphere interaction for a disk truncated just outside the corotation radius (Patruno et al. 2012).

solving the hydromagnetic force balance equation, subject to an integral flux-freezing constraint describing the confinement of accreted material to a polar flux tube. Throughout the paper, we adopt a barotropic equation of state (EOS) [model E in Priymak et al. (2011)], unless otherwise stated, which parametrises the various pressure contributions of a piecewise polytropic EOS into a convenient, M_a-dependent form and is a fair approximation to the realistic EOS. The equilibrium calculation is summarized in Section 2.1, an example solution is presented in Section 2.2, and the similarities and differences relative to previous work are summarized in section 2.3.

2.1 Grad-Shafranov equilibrium

We define a spherical coordinate system (r, θ, ϕ), where $\theta = 0$ is the magnetic symmetry axis before accretion begins. The magnetic field is given everywhere by

$$\boldsymbol{B} = \frac{\nabla\psi}{r\sin\theta} \times \hat{e}_\phi, \tag{1}$$

where $\psi(r,\theta)$ is a flux function. In the steady state, the magnetohydrodynamic (MHD) equations reduce to

$$\nabla P + \rho\nabla\phi + (\Delta^2\psi)\nabla\psi = 0, \tag{2}$$

where $\rho(r,\theta)$ is the mass density, P is the pressure, and Δ^2 denotes the Grad–Shafranov (GS) operator,

$$\Delta^2 = \frac{1}{4\pi r^2\sin^2\theta}\left[\frac{\partial^2}{\partial r^2} + \frac{\sin\theta}{r^2}\frac{\partial}{\partial\theta}\left(\frac{1}{\sin\theta}\frac{\partial}{\partial\theta}\right)\right]. \tag{3}$$

We adopt a general, barotropic equation of state of the form $P(\rho) = K\rho^\Gamma$, where Γ is the adiabatic index. For model E in Priymak et al. (2011), both Γ and K are scaled with M_a to emphasize the dominant pressure contributions acting within the mound. We then project equation (2) along $\boldsymbol{B}$, and solve for ψ by the method of characteristics. We find

$$\Delta^2\psi = -\frac{\mathrm{d}F(\psi)}{\mathrm{d}\psi}\left\{1 - \frac{(\Gamma-1)(\phi-\phi_0)}{\Gamma K^{1/\Gamma}[F(\psi)]^{(\Gamma-1)/\Gamma}}\right\}^{1/(\Gamma-1)}, \tag{4}$$

where $F(\psi)$ is an arbitrary function of the magnetic flux, and the gravitational potential near the surface takes the form $\phi(r) = GM_*r/R_*^2$, with $\phi_0 = \phi(R_*)$ at the stellar radius $r = R_*$.

To establish a one-to-one mapping between the initial (pre-accretion) and final (post-accretion) states that preserves the flux freezing condition of ideal MHD, we require that the final, steady-state, mass-flux distribution $\mathrm{d}M/\mathrm{d}\psi$ equals that of the initial state plus the accreted mass. This condition uniquely determines $F(\psi)$ through

$$\begin{aligned} F(\psi) \quad = \quad & \frac{K}{(2\pi)^\Gamma}\left(\frac{\mathrm{d}M}{\mathrm{d}\psi}\right)^\Gamma \\ & \times\left[\int_C \mathrm{d}s\; r\sin\theta|\nabla\psi|^{-1}\right. \\ & \left.\times\left\{1 - \frac{(\Gamma-1)(\phi-\phi_0)}{\Gamma K^{1/\Gamma}[F(\psi)]^{(\Gamma-1)/\Gamma}}\right\}^{1/(\Gamma-1)}\right]^{-\Gamma}. \end{aligned} \tag{5}$$

The above approach is self-consistent and therefore preferable to guessing $F(\psi)$ a priori (Hameury et al. 1983; Brown & Bildsten 1998; Melatos & Phinney 2001; Mukherjee & Bhattacharya 2012). Following earlier work, we prescribe the mass-flux distribution in one hemisphere to be

$$M(\psi) = \frac{M_\mathrm{a}[1-\exp(-\psi/\psi_\mathrm{a})]}{2[1-\exp(-b)]}, \tag{6}$$

where M_a is the accreted mass, ψ_* labels the flux surface at the magnetic equator, ψ_a labels the field line that closes just inside the inner edge of the accretion disk, and we write $b = \psi_*/\psi_\mathrm{a}$. In reality, $M(\psi)$ is determined by the details of the disk-magnetosphere interaction (Romanova et al. 2003, 2004), a topic outside the scope of this paper.

Equation (4) is solved simultaneously with equation (5) for $\psi(r,\theta)$ using an iterative under-relaxation algorithm combined with a finite-difference Poisson solver (Payne & Melatos 2004; Priymak et al. 2011). We adopt the following boundary conditions in keeping with previous work: $\psi(R_*,\theta) = \psi_*\sin^2\theta$ (surface dipole; magnetic line tying), $\mathrm{d}\psi/\mathrm{d}r(R_\mathrm{m},\theta) = 0$ (outflow), $\psi(r,0) = 0$ (straight polar field line), and $\mathrm{d}\psi/\mathrm{d}\theta(r,\pi/2) = 0$ (north-south symmetry), where $0 \leqslant r \leqslant R_\mathrm{m}$ and $0 \leqslant \theta \leqslant \pi/2$ delimit the computational volume. The outer radius R_m is chosen large enough to encompass the outer edge of the accreted matter. We place the line-tied inner boundary at $R_* = 10^6$ cm. The inner boundary is treated as a hard surface for simplicity; subsidence does not change the structure of the mountain radically (Choudhuri & Konar 2002; Wette et al. 2010). Convergence is achieved when the fractional grid-averaged ψ residual drops below 10^{-2}, typically after 10^3 iterations on a 256×256 grid (Payne & Melatos 2004).

2.2 Mound surface

Fig. 1 shows the output of the numerical GS solver for model E in Priymak et al. (2011) and $\psi_* = 1.6\times10^{24}$ G cm^2. The pre-accretion magnetic field is distorted significantly when the accreted mass exceeds a characteristic critical value (Priymak et al. 2011)

$$M_c = 8.1\times10^{-8}(\psi_*/10^{24}\text{ G cm}^2)^{4/3}\ M_\odot. \tag{7}$$

Throughout the paper, we set $\psi_* = 1.6\times10^{24}$ G cm^2, corresponding to a polar magnetic field strength of $10^{12.5}$ G, and take the neutron star mass to be $M_* = 1.4M_\odot$. The mountain in Fig. 1 is constructed for $M_a = M_c$. The thick black curve in the left panel denotes the outer surface of the mound $r = r_m(\theta)$ as a function of colatitude θ, i.e. the contour $\rho[r_m(\theta),\theta] = 0$. Dashed curves represent the density countours $\rho/\rho_\mathrm{max} = 0.1, 0.2$, normalized by the maximum density ρ_max at $(r,\theta) = (R_*,0)$. The thin blue curves describe contours of magnetic flux ψ, i.e. magnetic field lines. The right panel of Fig. 1 compares $|\mathbf{B}|$ at the mound surface as a function of θ (solid curve) with an undistorted dipole with the same hemispheric flux ψ_* (dotted curve). Magnetic burial reduces $|\mathbf{B}|$ by a factor of ≈ 6 at the pole and increases $|\mathbf{B}|$ by a factor of ≈ 2 at the equator relative to the dipole. In real systems, with $M_a \gg M_c$ typically, these factors are much higher. The reader is reminded that the asphericity ostensibly apparent in Fig. 1 is exaggerated by the choice of scale. The height of the mound changes by $\approx 10^4$ cm from $\theta \approx 60^\circ$ to 90°, over a lateral distance of $\approx 5\times10^5$ cm. Hence, to a good approximation, the surface

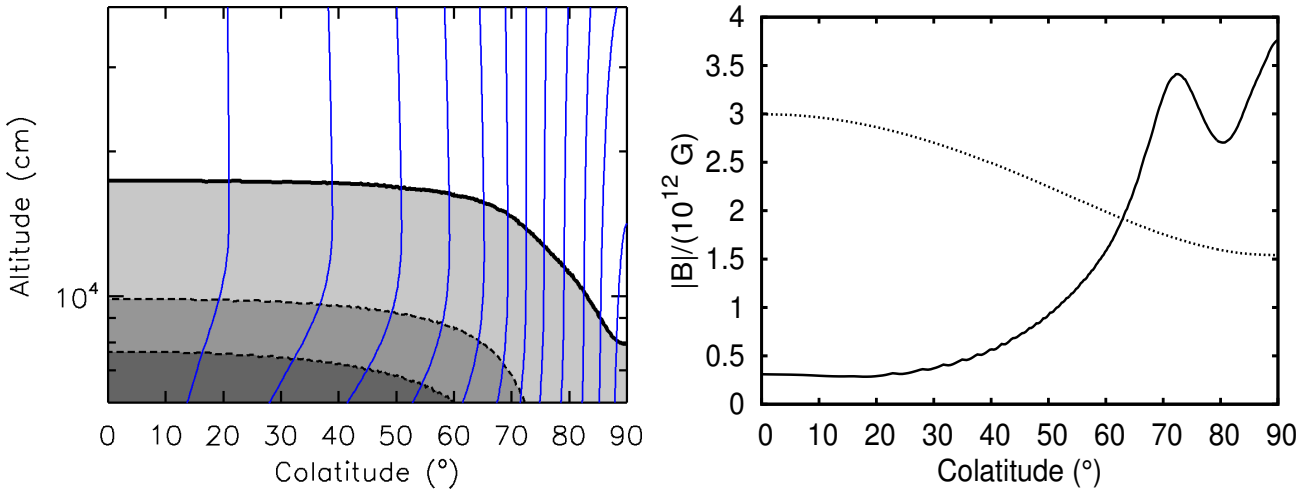

Figure 1. Equilibrium hydromagnetic structure of an accretion mound with $M_a = M_c$, $\psi_* = 1.6 \times 10^{24}$ G cm^2 and EOS model E (Priymak et al. 2011). (*Left panel*) Accretion mound surface $r = r_m(\theta)$ (thick solid curve) and magnetic field lines (ψ contours; thin blue solid curves) in a meridional plane of constant ϕ, with altitude $r - R_*$ and colatitude θ plotted on the vertical and horizontal axes respectively. Density contours are also drawn for $\rho = \eta\rho_{\max}$ with $\eta = 0.2, 0.1$ (dashed curves) and shaded accordingly. (*Right panel*) Magnetic field strength $|\mathbf{B}|$, in units of 10^{12} G, on the mound surface (solid curve) as a function of colatitude, compared to an undistorted magnetic dipole with $\psi_* = 1.6 \times 10^{24}$ G cm^2 (dotted curve).

is spherical, a property that we use to simplify the cyclotron line calculations in Section 3.

For a mound like the one in Fig. 1, one has $\mu \approx 0.5\mu_i$, much greater than observed in an LMXB. For realistic $M_a \sim 0.1M_\odot$ and $M_a/M_c \sim 10^6$, equation (7) does predict low enough μ, but then the structure in Fig. 1 needs to be modified: the equatorial belt is compressed into a narrower belt $80^\circ \lesssim \theta \lesssim 90^\circ$, with $B \gg 10^{13}$ G, and the field is buried at the pole, with $B \ll 10^{12}$ G and $\mathbf{B}$ almost latitudinal. Unfortunately, numerical limitations (including artificial bubble formation; see Section 8) of the GS method mean we cannot compute equilibria accurately for realistic $M_a \sim 0.1M_\odot$; this challenging issue besetting all the modeling to date (Brown & Bildsten 1998; Payne & Melatos 2004; Mukherjee & Bhattacharya 2012). Hence in this paper we do not claim that the predicted CRSF spectra are accurate but rather that they are indicative. In reality, the CRSF is dominated by $\mathbf{B}$ at a narrow range of latitudes where 10^{12} G $\lesssim B \lesssim 10^{13}$G, halfway between as B changes from $B \ll 10^{12}$ G at pole to $B \gg 10^{12}$ G at equator and this latitude range is narrower then the one that contributes to the CRSF spectra computed in this paper. We reiterate this important caveat (and return to the issue of magnetic bubbles) in Sec 8.

2.3 Comparison with previous work

The mound calculations in this paper deliberately parallel those in Mukherjee & Bhattacharya (2012) in many ways, although our specific goal — descriminating between thermal and magnetic mountains — differs from previous work. Both calculations assume magnetic linetying at a hard surface at $r = R_*$ [i.e. both papers neglect sinking; cf. Wette et al. (2010)], adopt a polytropic EOS, and assume that the mound is stable to ideal and resistive hydromagnetic modes, in line with the findings of time-dependent MHD simulations (Payne & Melatos 2007; Vigelius & Melatos 2008; Mukherjee et al. 2013b,c). The main differences arise in the geometry, the boundary condition at the equator, and the way flux freezing is treated. Mukherjee & Bhattacharya (2012) modeled the accretion mound within a polar cap of radius 1 km, and assumed cylindrical symmetry. In comparison, we model the mound over an entire hemisphere. We therefore capture fully the magnetic tension in the equatorially compressed magnetic field (Payne & Melatos 2004), which increases M_c by several orders of magnitude over previous estimates (Brown & Bildsten 1998; Litwin et al. 2001). Mukherjee & Bhattacharya (2012) adopted a strictly radial and uniform magnetic field at the surface, satisfying Dirichlet boundary conditions at the outer edge of the polar cap. We assume a dipolar magnetic field at the surface, and reflecting boundary conditions at the magnetic equator. Equatorial magnetic stresses stabilize the latter configuration against the growth of ideal-MHD ballooning modes for $M_a \lesssim M_c$ (Vigelius & Melatos 2008; Mukherjee & Bhattacharya 2012); cf. Litwin et al. (2001). Finally, we solve self-consistently for $F(\psi)$ through equation (5), whereas Mukherjee & Bhattacharya (2012) prescribed the mound height profile as a function of flux without connecting it to a plausible pre-accretion $M(\psi)$ via flux-freezing.

3 CRSF MODEL

The cyclotron spectrum emitted by a mound can be calculated in a few straightforward steps, once the magnetic field structure, temperature distribution, and surface contour of the mound, and the orientation of the star relative to the observer, are specified. We follow closely the method pioneered by Mukherjee & Bhattacharya (2012), who showed that cyclotron line formation occurs in a surface layer ~ 10 μm

thick. The key formulas underpinning each step of the calculation are summarized briefly in sections 3.1 (geometry), 3.2 (general relativistic light bending), 3.3 (line depth and width), and 3.4 (surface flux distribution), with an emphasis on the new features that are added. An example of a cyclotron spectrum is computed in Section 3.5 to illustrate the key features, e.g. phase evolution, which are studied further in Section 4.

3.1 Geometry

In keeping with Mukherjee & Bhattacharya (2012), we define a stationary (observer's) reference frame (X, Y, Z) as drawn in the left panel of Fig. 2, with origin O at the centre of the neutron star and Z-axis coincident with the rotation axis $\mathbf{\Omega}$, which does not precess by assumption [cf. Chung et al. (2008)]. In this frame, the colatitude and longitude of the line of sight (LOS) are ι and τ respectively, and the unit vector along the LOS is $\hat{\mathbf{n}}_o = (\sin\iota\sin\tau, \sin\iota\cos\tau, \cos\tau)$.

The accretion mound stands fixed on the surface of the star in a rotating reference frame (X', Y', Z'), where Z' is always aligned with the magnetic symmetry axis $\mathbf{M}$, and X coincides with X' at $t = 0$. The GS calculation (neglecting Coriolis and centrifugal forces)[2] is done in the primed frame (X', Y', Z') in a spherical coordinate system (r, θ, ϕ), where θ and ϕ are the colatitude and longitude with respect to $\mathbf{M}$, as in the left panel of Fig. 2. The axis $\mathbf{M}$ makes an angle α with respect to $\mathbf{\Omega}$. The angle $\omega(t)$ between X and X' in the $X - Y$ plane increases monotonically with t, as the star spins.

3.2 Ray tracing

Due to gravitational light bending, a ray intercepted by an observer along the LOS $\hat{\mathbf{n}}_o$ is emitted from a surface element on the mound at position $\mathbf{r}$ (shaded patch in the left panel of Fig. 2) along a unit vector $\hat{\mathbf{n}}_e$, which in general does not equal $\hat{\mathbf{n}}_o$. The right panel of Fig. 2 displays a magnified view of the emitting surface element. The angles between $\hat{\mathbf{n}}_o$ and $\hat{\mathbf{r}}$, and $\hat{\mathbf{n}}_e$ and $\hat{\mathbf{r}}$, are θ_o and θ_e respectively. They can be related via the approximate formula (Beloborodov 2002)

$$\cos\theta_e \approx u + (1-u)\cos\theta_o, \tag{8}$$

where $u = R_s/r$, and R_s is the Schwarzschild radius ($R_s \approx 4.1$ km for a neutron star with a fiducial mass of 1.4 $M_\odot$). This expression incorporates the effects of gravitational light bending to an accuracy of $\sim 1\%$ for typical neutron star parameters ($u \approx 1/3$). We set $u = 0.4$ throughout the paper. As the unit vectors $\hat{\mathbf{n}}_o$, $\hat{\mathbf{n}}_e$, and $\hat{\mathbf{r}}$ lie in the same plane, we can write

$$\hat{\mathbf{n}}_e = \frac{\sin(\theta_o - \theta_e)}{\sin\theta_o}\hat{\mathbf{r}} + \frac{\sin\theta_e}{\sin\theta_o}\hat{\mathbf{n}}_o. \tag{9}$$

[2] The ratio Λ of the Coriolis force to the Lorentz force satisfies $\Lambda \lesssim 10^{-8}$ for circulatory settling motions with speed $v \ll 1$ cm s^{-1} (Choudhuri & Konar 2002) and $\Lambda \lesssim 10^{-2}$ for a hypothetical zonal flow driven by accretion-induced temperature gradients [$v \lesssim 10^6$ cm s^{-1} even during a thermonuclear burst (Spitkovsky et al. 2002)], except perhaps near the pole, where the magnetic gradient is lower and $\Lambda \sim 1$ is possible. The centrifugal force is smaller than the Coriolis force by a factor $v/(R_*\Omega) \ll 1$.

To calculate the contribution to the observed cyclotron line profile from the surface element at $\mathbf{r}$, we need to know the angle between $\hat{\mathbf{n}}_e$ and the unit vector parallel to the local magnetic field, $\hat{\mathbf{n}}_b = \mathbf{B}/|\mathbf{B}|$. The GS calculation in Section 2 yields $\hat{\mathbf{n}}_b$ as well as the mound surface contour $r = r_m(\theta)$ in the frame (X', Y', Z'). We therefore apply Euler rotations to $\hat{\mathbf{n}}_o$ about the Z and X axes by angles $-\omega(t)$ and $-\alpha$ respectively (see left panel of Fig. 2) to bring it into the body frame (X', Y', Z') (i.e. $\hat{\mathbf{n}}_o$ depends on t in the body frame). We then use equation (9) to calculate $\hat{\mathbf{n}}_e(r, \theta, \phi, t)$ at $\mathbf{r}$ in the body frame.

3.3 Line shape

The angle θ_{eb} between $\hat{\mathbf{n}}_e$ and $\hat{\mathbf{n}}_b$ determines the line energy, width, and depth of a CRSF feature. The central energy of a cyclotron line of order n is given by

$$E_{\rm cyc,n} = m_e c^2 (1-u)^{1/2} \mathrm{cosec}^2\theta_{eb} \times \{[1 + 2n(B/B_{\rm crit})\sin^2\theta_{eb}]^{1/2} - 1\}, \tag{10}$$

where m_e is the electron rest mass, c is the speed of light, $B_{\rm crit} = m^2c^3/(e\hbar) \approx 4.4\times10^{13}$G is the critical field strength, and the factor $(1-u)^{1/2}$ arises from the gravitational redshift. We only study the fundamental ($n = 1$) cyclotron line in this paper. Since we have $B/B_{\rm crit} \lesssim 10^{-1}$ at the mound surface, where most of the flux is emitted (see Fig. 1), we expand equation (10) to first order in $B/B_{\rm crit}$ to give:

$$E_{\rm cyc}(\theta_{eb}, B) = E_0(1-u)^{1/2}\left[1 - \left(\frac{E_0}{1.02\,\mathrm{MeV}}\right)\sin^2\theta_{eb}\right], \tag{11}$$

with $E_0 = 11.6(B/10^{12}$ G) in keV. Priymak et al. (2011) found $B/B_{\rm crit}$ as high as $\sim 10^2$ in parts of the accretion mound, but these regions lie well beneath the thin emitting skin at the surface for all relevant EOS models.

We assume isotropic emission at each point on the surface [i.e. $F(\theta_e, E, \theta_{eb}) = F(E, \theta_{eb})$], and simplify the emitted spectrum in the vicinity of $E_{\rm cyc}$ as a flat continuum (of unit flux) modulated by the CRSF [cf. Coburn et al. (2002)], which is assumed to be a Gaussian in absorption:

$$F(E, \theta_{eb}) = 1 - [1 - D(\theta_{eb})]\exp\Big[-\frac{2.8(E - E_{\rm cyc})^2}{F(\theta_{eb})^2}\Big]. \tag{12}$$

Here, $D(\theta_{eb})$ is the line depth, and $F(\theta_{eb})$ is the full width half maximum. Equation (12) is not strictly correct, because a typical CRSF profile is more complicated than a Gaussian (Kreykenbohm et al. 2005; Schönherr et al. 2007), but we follow Mukherjee & Bhattacharya (2012) in adopting the Gaussian approximation.

The line width $F(\theta_{eb})$ and depth $D(\theta_{eb})$ are obtained directly from Fig. 8 of Schönherr et al. (2007), for a slab 1-0 geometry (plane parallel homogeneous layer illuminated from below). A slab is a fair approximation to a small element on the mound surface, whereas a cylindrical geometry is more appropriate for the accretion column as a whole. The spectral contribution arising from fan-beam emission from a radiation-dominated accretion column should not be ignored for supercritical accretors with accretion luminosities comparable to the Eddington luminosity (Basko & Sunyaev 1976; Nelson et al. 1993; Becker et al. 2012). In this paper, for simplicity, we model the cyclotron spectra exclusively

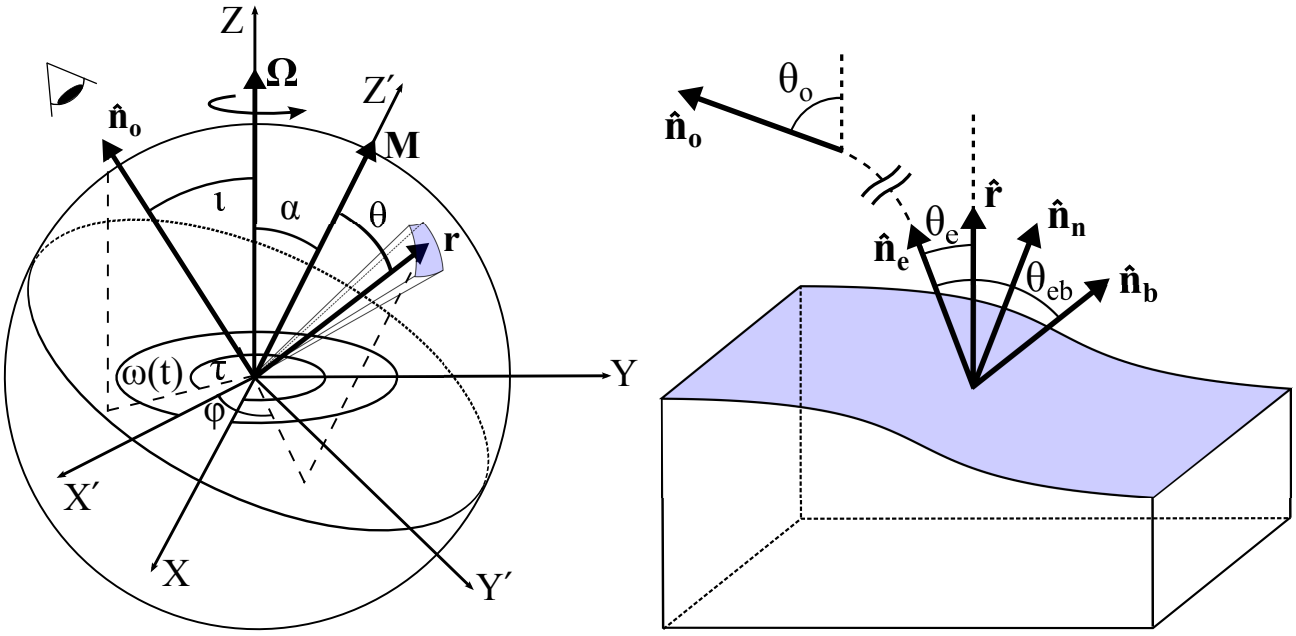

Figure 2. (*Left panel*) Orientation of the body frame (X', Y', Z') relative to the observer's frame (X, Y, Z). The Z'-axis is aligned with the magnetic symmetry axis $\mathbf{M}$ and inclined by an angle α with respect to $\mathbf{\Omega}$. The primed frame rotates about $\mathbf{\Omega}$. The position vector $\mathbf{r}$ to a surface element has colatitude θ and longitude ϕ in the primed frame. The line of sight $\hat{\mathbf{n}}_o$ makes angles ι and τ with the Z axis and X axis in the X–Y plane. (*Right panel*) Magnified view of the local surface of the accretion mound, showing the unit emission vector $\hat{\mathbf{n}}_e$, unit radial vector $\hat{\mathbf{r}}$, unit surface normal $\hat{\mathbf{n}}_n$, unit magnetic field vector $\hat{\mathbf{n}}_b$, and the angles between them. Due to gravitational light bending, photons emitted along $\hat{\mathbf{n}}_e$ follow a curved path (interrupted dashed curve) and are ultimately observed along $\hat{\mathbf{n}}_o$. In general, one has $\hat{\mathbf{n}}_n \cdot \hat{\mathbf{r}} \neq 1$ due to asphericity of the accretion mound, but $\hat{\mathbf{n}}_n \cdot \hat{\mathbf{r}} \approx 1$ holds to a good approximation. The vectors $\hat{\mathbf{r}}$, $\hat{\mathbf{n}}_b$, $\hat{\mathbf{n}}_l$, $\hat{\mathbf{n}}_e$ lie in the same plane for axisymmetric GS equilibria (see Section 2.1).

from subcritical accretors, which are often the subject of gravitational-wave studies, and do not consider cylindrical geometry any further. The slab 1-1 geometry (plane parallel homogeneous layer illuminated at the mid plane) yields qualitatively similar results to 1-0, because $F(\theta_{eb})$ and $D(\theta_{eb})$ have similar functional forms in the two cases [see Fig. 8 of Schönherr et al. (2007)]. Given the inability of current observations to discriminate between 1-0 and 1-1, we do not consider the 1-1 geometry further.

3.4 Surface flux

We divide the neutron star surface into equal-area elements $\Delta A_{\theta_i,\phi_j}$ at latitude θ_i and longitude ϕ_j. The observed spectrum is constructed by numerically integrating the emitted spectrum $F(E, \theta_{eb})$ from equation (12) over the observable $(\hat{\mathbf{n}}_e \cdot \hat{\mathbf{n}}_n > 0)$ grid elements and multiplying by the projected area perpendicular to the LOS:

$$F_{tot}(E) = \sum_{\theta_i,\phi_j} F[E, \theta_{eb}(\theta_i, \phi_j)] \Delta A(\theta_i, \phi_j) \cos\theta_e. \qquad (13)$$

For plotting purposes, we normalize the integrated spectrum from equation (13) to give unit peak flux. Strictly speaking, the surface of the accretion mound is not spherical. Hence the unit normal $\hat{\mathbf{n}}_n$ of any surface element does not equal the unit position vector $\hat{\mathbf{r}}$ of that element (see right panel of Fig. 2). In this paper, however, we make the approximation $\hat{\mathbf{n}}_n \approx \hat{\mathbf{r}}$, which is accurate everywhere [maximum $\sim 1\%$ error at $\theta \approx \pi/2$; see Fig. 1], as $\hat{\mathbf{n}}_n$ is hard to calculate accurately from the numerical GS output.

3.5 Worked example

Figure 3 (left panel) shows the spectrum emitted by the accretion mound of Fig. 1 when it is observed from the vantage point $\iota = \pi/4,\ \tau = 0$ with magnetic inclination $\alpha = \pi/6$. The spectrum is plotted at three phases $(\omega = 0,\ 2\pi/3,\ 4\pi/3)$. Also shown in the right panel is the spectrum at the same phases before accretion ($M_a = 0$), when the magnetic field is an undisturbed dipole. In the next two figures, to aid interpretation, we compute the line parameters $E_{\rm cyc}$, F, and D (Figure 4) and direction cosines $\hat{\mathbf{n}}_e \cdot \hat{\mathbf{r}}$, $\hat{\mathbf{n}}_e \cdot \hat{\mathbf{n}}_o$, and $\hat{\mathbf{n}}_e \cdot \hat{\mathbf{n}}_b$ (Figure 5) as functions of colatitude θ and longitude ϕ in the body frame for the same three rotational phases $\omega = 0,\ 2\pi/3,\ 4\pi/3$ (top to bottom rows).

The cyclotron spectrum from an undistorted magnetic dipole (right panel of Fig. 3) exhibits a single absorption trough at $E_{\rm cyc} \approx 20$ keV. It is approximately phase invariant, the line properties change by $\Delta E_{\rm cyc} \approx 5$ keV, $\Delta F \approx 3$ keV, and $\Delta D \approx 10^{-4}$ over one rotation period. In comparison, the spectrum generated from the surface of the accretion mound (left panel of Fig. 3) displays two distinct CRSFs at $E_{\rm cyc,1} \approx 5$ keV and $E_{\rm cyc,2} \approx 27$ keV with $\Delta E_{\rm cyc,1} \approx 1$ keV, $\Delta F_1 \approx 5$ keV, $\Delta D_1 \approx 5 \times 10^{-3}$, and $\Delta E_{\rm cyc,2} \approx 2$ keV, $\Delta F_2 \approx 5$ keV, $\Delta D_2 \approx 5 \times 10^{-4}$. The solid black curves in Fig. 4 and red shading in the left column of Fig. 5 show that more than half the surface contributes to the observed spectrum $(\hat{\mathbf{n}}_e \cdot \hat{\mathbf{r}} > 0)$ due to gravitational light bending. The angle $\theta_o - \theta_e$ increases as $\hat{\mathbf{r}}$ tilts away from $\hat{\mathbf{n}}_o$ [see equations (8) and (9)] and is rarely greater than $\approx 60^\circ$ (see middle column of Fig. 5). Although the unit magnetic field vectors $\hat{\mathbf{n}}_b$ are always axisymmetric (in this

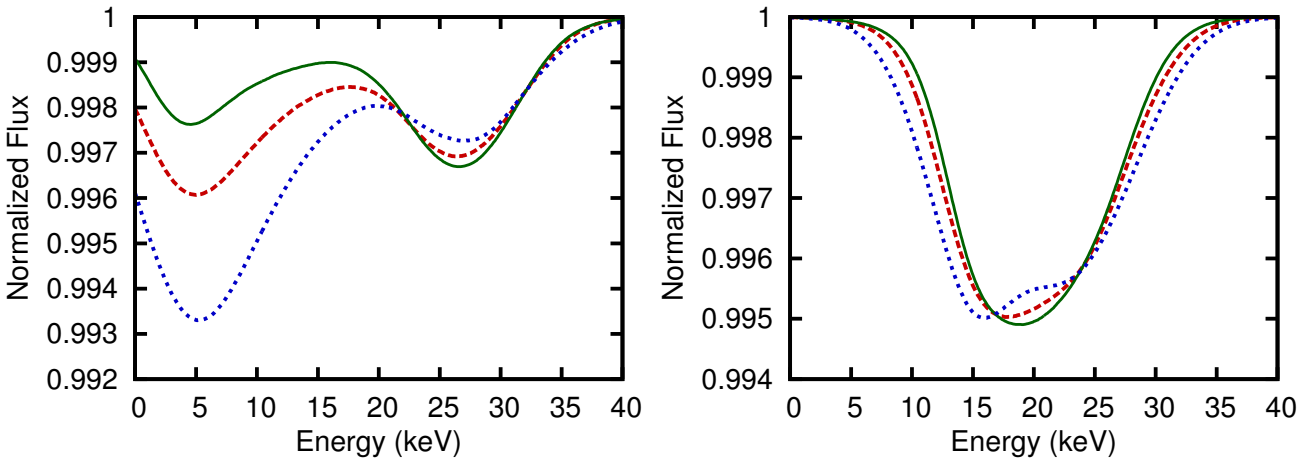

Figure 3. Phase-dependent normalized CRSF spectrum with $(\iota, \alpha) = (\pi/4, \pi/6)$, $\psi_* = 1.6 \times 10^{24}$ G cm^2, and $u = 0.4$. (*Left panel*) Magnetic mountain with $M_a = M_c$ and EOS model E (Priymak et al. 2011). (*Right panel*) Undisturbed magnetic dipole with $M_a = 0$. The three curves in each panel correspond to three rotational phases: $\omega = 0$ (dashed red), $2\pi/3$ (solid green), and $4\pi/3$ (dotted blue).

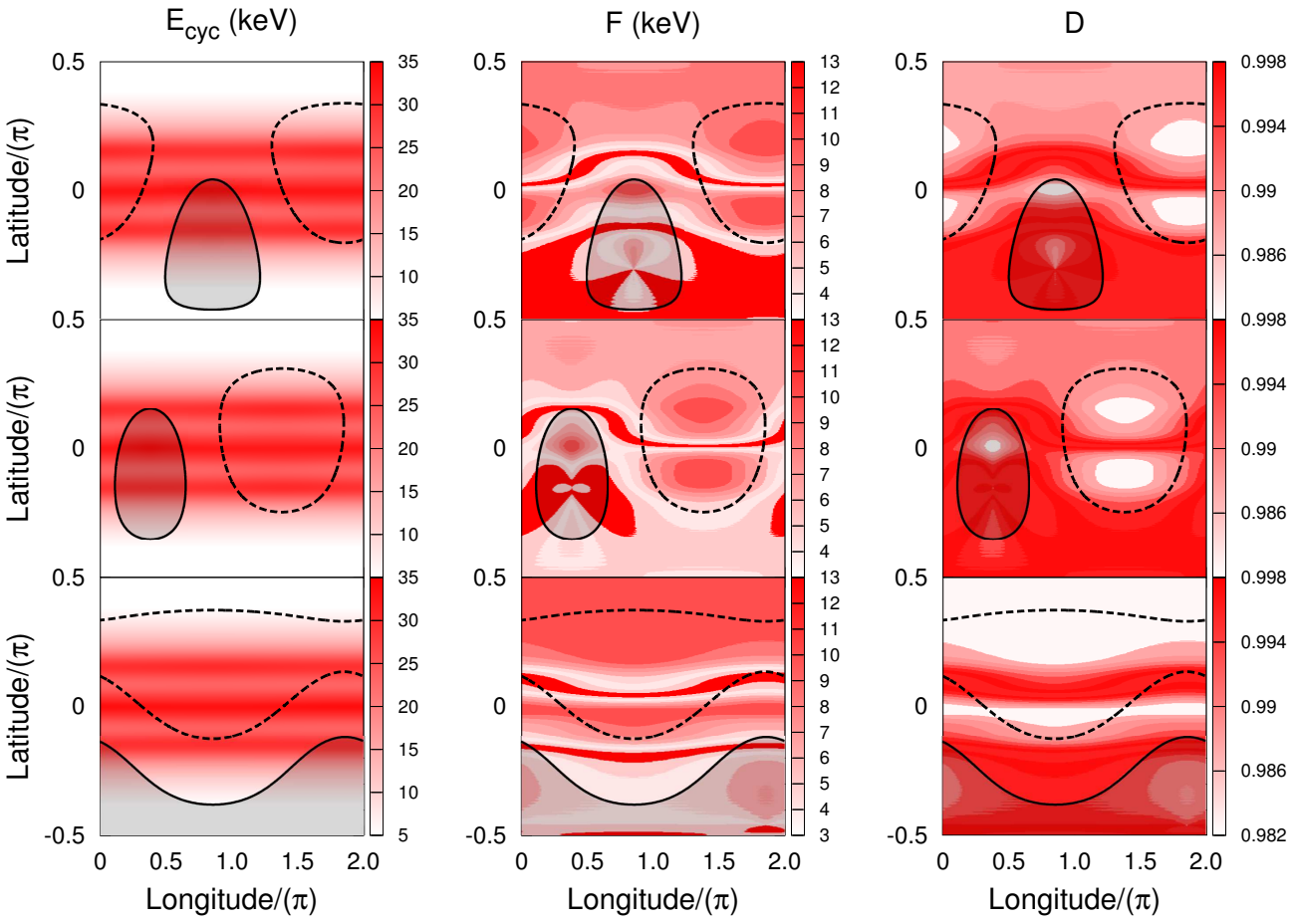

Figure 4. Surface variation of CRSF parameters $E_{\rm cyc}$ (line energy in keV), F (full width half maximum in keV), and D (depth in normalized flux units) (left to right columns) as functions of rotational phase $\omega = 0,\ 2\pi/3,\ 4\pi/3$ (top to bottom rows) with $(\iota, \alpha) = (\pi/4, \pi/6)$, $\psi_* = 1.6 \times 10^{24}$ G cm^2, $u = 0.4$, $M_a = M_c$, and EOS model E (Priymak et al. 2011). The vertical and horizontal axes represent latitude $\pi/2 - \theta$ and longitude ϕ respectively, in units of π radians. The magnitude of the plotted parameters is described by the red shading, with minimum/maximum values plotted as light/dark respectively. Regions on the surface which do not contribute to the observed spectrum ($\hat{\mathbf{n}}_e \cdot \hat{\mathbf{r}} \leqslant 0$) and which dominate the surface-integrated cyclotron spectrum, i.e. $(\hat{\mathbf{n}}_e \cdot \hat{\mathbf{r}})\mathrm{d}A \geqslant \max[(\hat{\mathbf{n}}_e \cdot \hat{\mathbf{r}})\mathrm{d}A]/2$, are enclosed by solid and dashed black curves respectively.

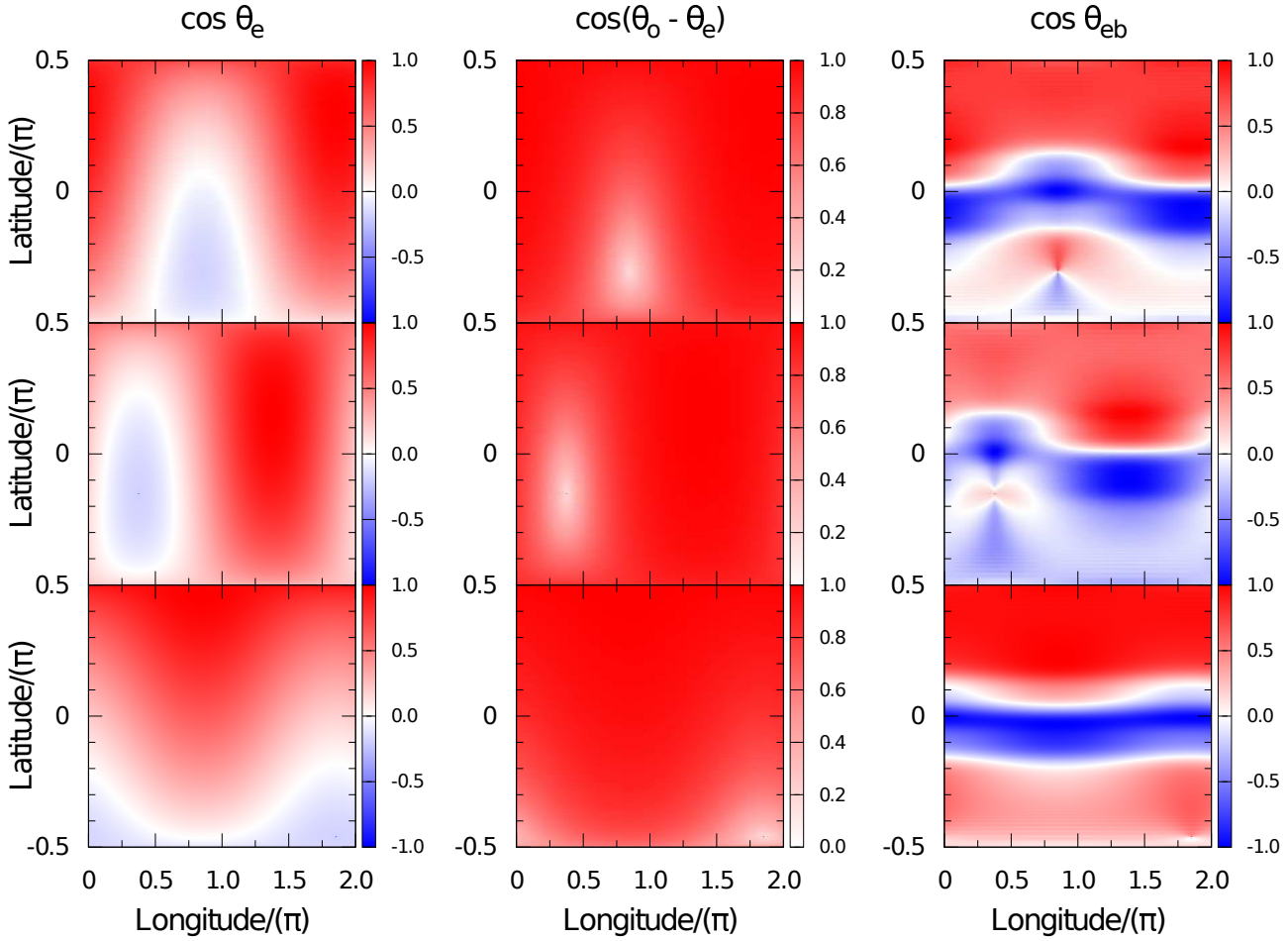

Figure 5. Surface variation of direction cosines $\cos\theta_e$, $\cos(\theta_o - \theta_e)$, and $\cos\theta_{eb}$ (left to right columns) as functions of rotational phase $\omega = 0,\ 2\pi/3,\ 4\pi/3$ (top to bottom rows) with $(\iota, \alpha) = (\pi/4, \pi/6)$, $\psi_* = 1.6 \times 10^{24}$ G cm^2, $u = 0.4$, $M_a = M_c$, and EOS model E (Priymak et al. 2011). The vertical and horizontal axes represent latitude $\pi/2 - \theta$ and longitude ϕ respectively, in units of π radians. The magnitude of the plotted direction cosines is described by the red shading, with minimum/maximum values plotted as light/dark respectively.

specific GS geometry), the emission unit vectors $\hat{\mathbf{n}}_e$ are not axisymmetric for non-trivial $\hat{\mathbf{n}}_o$ and $\mathbf{M}$ orientations, as θ_{eb} depends on ϕ and t (rightmost column of Fig. 5). As a corollary, the region on the surface which dominates the flux, i.e. $(\hat{\mathbf{n}}_e \cdot \hat{\mathbf{r}})\mathrm{d}A \geqslant \max[(\hat{\mathbf{n}}_e \cdot \hat{\mathbf{r}})\mathrm{d}A]/2$ (see dashed black curves in Fig. 4), is similarly non-axisymmetric and phase-dependent.

The appearance of two narrow absorption features from a mountain is explained by the contribution of both the compressed equatorial magnetic field (at ≈ 27 keV from latitude $0 \lesssim |\pi/2 - \theta| \lesssim 0.3\pi$) and the diluted polar magnetic field (at ≈ 5 keV from latitudes $0.3\pi \lesssim |\pi/2 - \theta| \lesssim \pi$) (leftmost column of Fig. 4). The line at $E_{\mathrm{cyc},1}$ is the dominant absorption feature for $2\pi/3 \leqslant \omega \leqslant 2\pi$ because a larger fraction of the polar region contributes to the surface-integrated flux for $2\pi/3 \lesssim \omega \lesssim 4\pi/3$ than for $0 \lesssim \omega \lesssim 2\pi/3$. You can see this in Fig. 5 by comparing the areas enclosed by the dashed black curves in the top, middle, and bottom panels. Here the polar region is that where the distorted magnetic field is approximately parallel to the emission direction $(\hat{\mathbf{n}}_e \cdot \hat{\mathbf{n}}_b \approx 1)$; see leftmost and rightmost columns of Fig. 5.

The line depth D varies substantially over one full rotation period (rightmost column of Fig. 4 and leftmost column of Fig. 5), especially for the line at $E_{\mathrm{cyc},1}$ ($\Delta D_1 \approx 5 \times 10^{-3}$). The line $E_{\mathrm{cyc},1}$ is generated primarily in the polar regions, and θ_{eb} in this region varies with rotational phase (see rightmost column of Fig. 5). Since D and F are directly related to $\cos\theta_{eb}$ at each emission point, in such a way that there exists a monotonic correlation between them [see middle and rightmost columns of Fig. 4 and Schönherr et al. (2007)], we expect to see some part of that correlation survive after integrating over the observable area $(\hat{\mathbf{n}}_e \cdot \hat{\mathbf{r}} > 0)$, so that the line is widest when it is deepest, and vice versa.

4 ORIENTATION

The detailed shape of a CRSF and its variation with rotational phase depend on the magnetic inclination α and the observer's inclination ι. In this section we show that phase-resolved CRSF observations can constrain α and ι (without fixing them uniquely; e.g. the spectrum is unchanged when switching α and ι). As well as assisting with studies of surface structure, this capability may play a role in future in

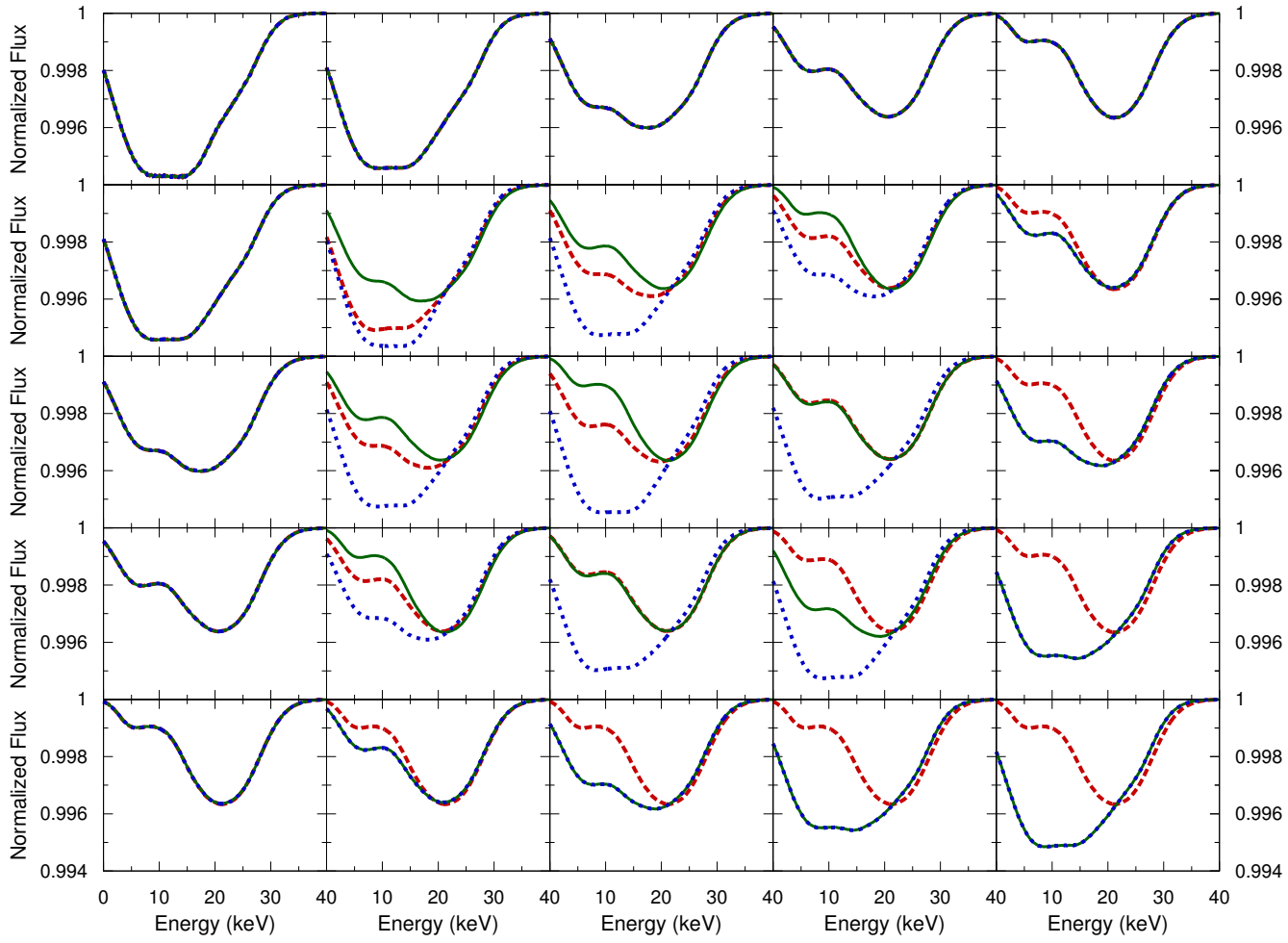

Figure 6. Phase-resolved normalized CRSF spectra for a magnetic mountain with $M_a = 0.75M_c$, $u = 0.4$, $\psi_* = 1.6 \times 10^{24}$ G cm^2, and EOS model E (Priymak et al. 2011), covering a range of observer inclination angles $\iota = 0$, $\pi/8$, $\pi/4$, $3\pi/8$, $\pi/2$ (top to bottom rows) and magnetic inclination angles $\alpha = 0$, $\pi/8$, $\pi/4$, $3\pi/8$, $\pi/2$ (left to right column). In each panel, three phases ($\omega = 0$, $2\pi/3$, $4\pi/3$) are plotted as long-dashed red, solid green, and dotted blue curves respectively.

reducing the parameter space for computationally expensive gravitational wave searches. Constraining α and ι is the first step in discriminating between thermal and magnetic mountains in various systems, as described in Section 7.

The spectrum emitted by a mound of mass $M_a = 0.75M_c$ is displayed in Figure 6, for different observer orientations ($\iota = 0, \pi/4, 3\pi/8, \pi/2$, top to bottom rows), inclination angles ($\alpha = 0, \pi/4, 3\pi/8, \pi/2$, top to bottom rows), and rotational phases $\omega = 0, 2\pi/3, 4\pi/3$ (long-dashed red, solid green, and dotted blue curves respectively). We set $\tau = 0$ for convenience; τ simply introduces a phase offset.

For $\alpha = 0$ (left column) and $\iota = 0$ (top row), the spectrum is independent of phase. Emission from the region $55^\circ \lesssim \theta \lesssim 65^\circ$ dominates the overall spectrum, weighted by the factor $\cos\theta_e(\theta)\,\mathrm{d}A(\theta)$. The relatively wide and deep CRSF at $(\iota, \alpha) = (0, 0)$ separates into two distinct absorption troughs as ι or α increase, and the troughs simultaneously become shallower. Emission from the polar cap dominates the spectrum at $(\iota, \alpha) = (0, 0)$. The equatorial belt ($70^\circ \lesssim \theta \lesssim 90^\circ$) contributes more, as either ι or α increase. Since $|\mathbf{B}|$ is greater in the equatorial belt than at the pole, the deeper trough shifts to higher energies, while the shallower trough shifts to lower energies, as accreted matter spreads equatorward and $|\mathbf{B}|$ at the pole weakens (see Fig. 1). The line depth falls with ι or α because θ_{eb} increases on average over the region $\hat{\mathbf{n}}_e \cdot \hat{\mathbf{r}} > 0$ [see Fig. Schönherr et al. (2007)].

When neither ι nor α are near zero, it is harder to draw definite conclusions about the viewing geometry from observations. Nevertheless, some constraints can be deduced. If either ι or α approaches $\pi/2$, the spectrum transitions between two distinct states within one period, at twice the rotational frequency. In contrast, for $\pi/8 \lesssim \iota, \alpha \lesssim 3\pi/8$, the spectrum transitions between three states within one period, if sampled at three equally spaced rotational phases. This information, albeit incomplete, is potentially useful for surface magnetic field reconstruction and for optimizing gravitational-wave searches.

5 ACCRETED MASS

The accreted mass M_a in observed systems cannot be measured directly and is usually estimated via evolutionary

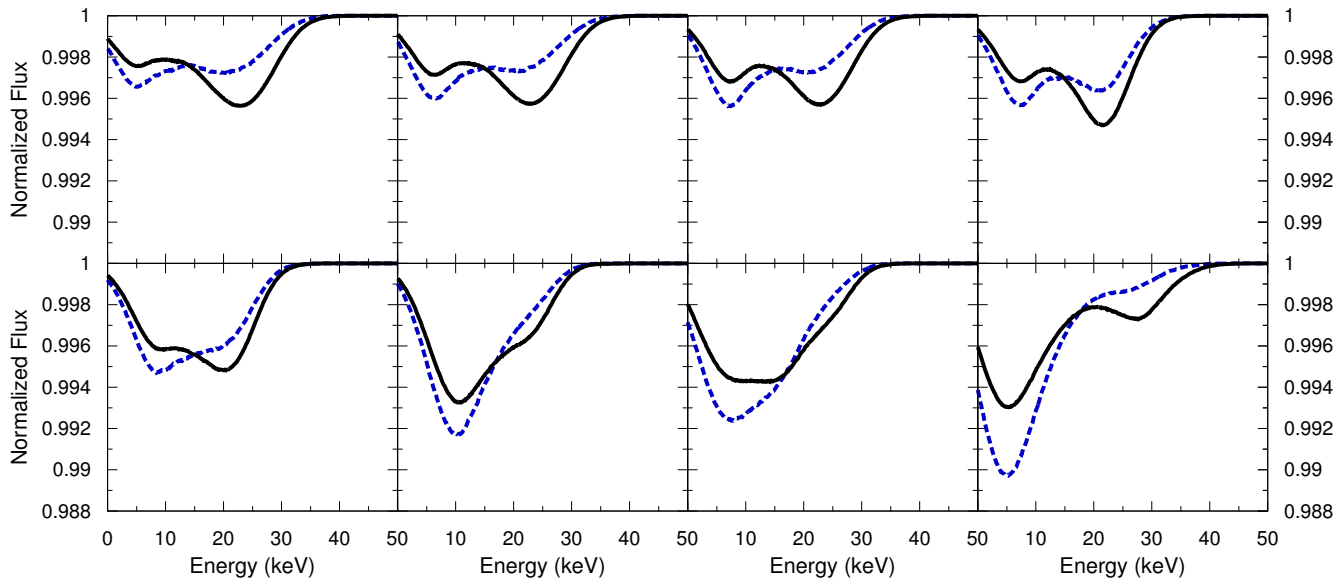

Figure 7. CRSF spectra for a magnetic mountain in the aligned configuration $(\iota, \alpha) = (0, 0)$ (i.e. no phase dependence), with $u = 0.4$, $\psi_* = 1.6 \times 10^{24}$ G cm^2, and EOS model E (Priymak et al. 2011), as a function of accreted mass $M_a/M_c = 10^{-4}$, 10^{-3}, 10^{-2}, 10^{-1} (top row, left to right column), and $M_a/M_c = 0.25$, 0.5, 0.75, 1.0 (bottom row, left to right column). In each panel, the solid and dashed curves correspond to uniform and nonuniform, magnetic-pressure modified surface temperature distributions respectively.

studies (Podsiadlowski et al. 2002; Pfahl et al. 2003). $|\mathbf{B}|$ and the ellipticity ϵ of the star are partly determined by M_a (with lesser contributions from the specific accretion geometry and the EOS); both are important properties of the accretion mound's structure. In addition, ϵ determines the characteristic strain h_0 of the gravitational wave signal. It is therefore useful to both magnetic field and gravitational wave studies to examine how M_a affects the cyclotron spectrum. A detection of CRSFs in an accreting neutron star can, in principle, constrain M_a and hence help predict ϵ and h_0.

Fig 7 presents the spectrum generated by EOS model E (solid black curve) for a mound with constant surface temperature $T = 3.5 \times 10^7$ K (Schönherr et al. 2007) for an aligned configuration with $(\iota, \alpha) = (0, 0)$ and hence no phase dependence, $u = 0.4$, and $\psi_* = 1.6 \times 10^{24}$G cm^2. The spectrum is plotted in eight panels as a function of M_a, with $M_a/M_c = 10^{-4}$, 10^{-3}, 10^{-2}, 10^{-1} along the top row (left to right), and $M_a/M_c = 0.25$, 0.5, 0.75, 1.0 along the bottom row (left to right).

As accretion proceeds, the magnetic field at the surface of the mound is increasingly distorted. For $M_a \lesssim 10^{-1}\ M_c$, both troughs deepen as M_a increases, because the angle θ_{eb} increases over the observed area, as $\mathbf{B}$ is compressed laterally. For $M_a \gtrsim 10^{-1}\ M_c$, the monotonic trend ceases, and the line at $E_{\rm cyc,1}$ becomes deeper than the line at $E_{\rm cyc,2}$. For $0.5 \leqslant M_a/M_c \leqslant 0.75$, in the two central panels of the bottom row in Fig. 7, the troughs merge. This coincides with the start of the nonlinear trend in magnetic dipole moment versus M_a; see Figure 11 in Priymak et al. (2011). The separation in line energy $E_{\rm cyc,2} - E_{\rm cyc,1}$ decreases monotonically with M_a for $M_a \ll M_c$, but the trend breaks down for $M_a \gtrsim 0.75 M_c$ for the same reason.

In reality, the temperature distribution at the surface of the accretion mound is not uniform; the temperature is lower than it would otherwise be, wherever $|\mathbf{B}|$ is higher, because the magnetic field provides pressure support, like in a Solar sunspot (Priest 1982). A full calculation of thermal transport lies outside the scope of this paper. To estimate the effect crudely, we multiply the flux emitted from each surface point by the Stefan-Boltzmann correction factor (Priest 1982)

$$\lambda(\theta) = \left\{1 - \beta \mathbf{B}[r_m(\theta), \theta]^2\right\}^4, \tag{14}$$

where $\beta \propto (\rho T_0)^{-1}$ depends on the temperature T_0 at the pole. The second term in braces equals the ratio of the magnetic pressure at colatitude θ to the kinetic pressure at the pole, where $|\mathbf{B}|$ is small. It is always positive for the typical magnetic fields and temperatures (10^{12} G $\lesssim |\mathbf{B}| \lesssim 10^{13}$ G, $T_0 \sim 10^8$ K) relevant to CRSF formation in accreting neutron stars. Equation (14) expresses the constancy of the total (kinetic plus magnetic) pressure in MHD equilibrium but does not take into account corrections due to additional, ongoing, accretion-driven heating.

The results of applying the correction factor (14) to cyclotron spectra are presented in Fig. 7 as blue dashed curves. In comparison to accretion mounds with uniform surface temperature, the 'sunspot' effect suppresses the absorption feature at $E_{\rm cyc,2}$ and augments the feature at $E_{\rm cyc,1}$. The $E_{\rm cyc,2}$ line originates near the magnetic equator, where $|\mathbf{B}|$ is enhanced by burial and T is lower, whereas the $E_{\rm cyc,1}$ line originates near the magnetic pole, where T reaches its maximum value T_0 (see Fig. 1).

The above results suggest one qualitative way to discriminate between magnetic and thermal mountains in different classes of accreting neutron stars. The cyclotron spectrum of a magnetic mountain depends strongly on M_a, whereas the spectrum of a thermal mountain depends mainly on accretion-driven heating, i.e. $\dot{M}$ and the hot-spot geometry (Ushomirsky et al. 2000). In young accretors, where insufficient mass has accreted to completely bury the magnetic field below the crust, the CRSFs may evolve on

the burial time-scale $M_c/\dot{M} \sim 10^2$–10^3 yr. Such evolution may be detectable over the next decade with next-generation X-ray telescopes. In contrast, CRSFs from thermal mountains should remain more stable. Needless to say, much more work (e.g. on thermal transport) is needed to establish the practicality of this idea.

6 EQUATION OF STATE

In this section we examine how the EOS of the magnetized mound affects the cyclotron spectrum, to scope out the range of possibilities. For the sake of definiteness, we analyse the polytropic EOS models B–D in Priymak et al. (2011), describing the various degenerate pressures in the neutron star crust, as well as an isothermal and mass-weighted EOS (models A and E respectively).

In Figure 8 we plot spectra from mounds for models A (dot-dashed red curve), B (short-dashed blue curve), C (dotted purple curve), D (long-dashed green curve), and E (solid black curve) as a function of M_a, with $M_a/M_c = 10^{-4}$, 10^{-3}, 10^{-2}, 10^{-1} (top row, left to right column), and $M_a/M_c = 0.25$, 0.5, 0.75, 1.0 (bottom row, left to right column). The aligned configuration $(\iota, \alpha) = (0, 0)$ is chosen deliberately to suppress the phase dependence, as in Fig. 7.

At each M_a, there are subtle differences in the spectra produced by different models. The differences arise because the EOS affects the overall magnetic structure of the mound; thermal EOS effects confined to the thin, X-ray-emitting skin of the mound are negligible. Model A behaves qualitatively differently to models B–D. For $M_a \ll M_c$, model A exhibits a single absorption trough, whereas models B–D exhibit two. As M_a rises to $\approx 0.5M_c$, the trough in model A becomes narrower, deeper, and shifts to lower energy. On the other hand, the troughs in models B–D approach equal depths and subsequently merge. For $M_a \gtrsim 0.5M_c$, model A splits into two distinct absorption features, whose energy separation increases with M_a, with the lower energy feature becoming more prominent. In comparison, for models B–D, the CRSF splits into two, and the lower energy feature dominates, as M_a increases.

The ellipticity ϵ is plotted as a function of accreted mass M_a (in solar masses) for models A–E in Fig. 9. The results follow the approximate scaling $\epsilon = (M_a/M_\odot)(1+M_a/M_c)^{-1}$ (Melatos & Payne 2005; Vigelius & Melatos 2009). Since M_c varies by a factor of $\sim 10^4$ between the models, so too does the value where ϵ saturates in Fig. 9. The $\epsilon(M_a)$ relation in the figure, and the scaling of magnetic dipole moment μ with M_a presented elsewhere (Payne & Melatos 2004; Priymak et al. 2011), combine to imply a relation $\mu(\epsilon)$ which is observationally testable in principle, if ϵ can be inferred from CRSF studies or a gravitational wave measurement (if the spin period and source distance are known). By comparing observed cyclotron spectra with those predicted by models A–E as functions of M_a, we can, in principle, extract information on the EOS of the accreted matter, stellar orientation, and surface magnetic field. As in Section 5, however, there is a long way to go to establish the practicality of multimessenger investigations of this kind.

7 DISCRIMINATING BETWEEN THERMAL AND MAGNETIC MOUNTAINS

Mountains on accreting neutron stars are sustained either by magnetic stresses, as in Section 2, or by thermoelastic stresses maintained by temperature gradients (e.g. from inhomogeneous heating in the crust), as discussed in Section 1. Temperature gradients can also drive compositional gradients, e.g. 'wavy' electron capture layers (Bildsten 1998; Ushomirsky et al. 2000). In this section we compare the signatures left by thermal and magnetic gradients on the cyclotron spectrum and suggest observational methods for discriminating between them. This is potentially interesting for studies of the surface magnetic structure of accreting neutron stars and also for objects that may be detected in future as gravitational wave sources. The discussion is preliminary; a detailed exploration of the problem and its parameter space will be presented elsewhere (Haskell et al. 2014, in preparation). We emphasize again that the CRSFs calculated below and elsewhere in this paper are too weak to be detected by currently operational X-ray telescopes. The results in this section are a first attempt to think through what could be achieved by multimessenger observational strategies in the context of thermal and magnetic mountains in the future.

7.1 Scenarios

Consider the four generic scenarios below for generating a mountain with ellipticity ϵ by accretion.

(a) Thermal gradients dominate ϵ, and the process of magnetic burial described in Section 2.1 (mound spreads equatorward, $\mathbf{B}$ is compressed at the equator) does not occur. Upon decomposing the temperature perturbation $\delta T = \sum_{l,m} \delta T_{lm}(r) Y_{lm}(\theta, \phi)$ into spherical harmonics Y_{lm}, with $T = T_0(1+\delta T)$, we note that we can relate δT to ϵ if δT_{20} is the dominant term; see Ushomirsky et al. (2000). δT also modulates the surface X-ray flux and hence the instantaneous and phase-averaged cyclotron spectra.

(b) Thermal gradients dominate ϵ, but magnetic burial does occur. Then the cyclotron spectrum (but not ϵ) is modified by magnetic burial.

(c) Magnetic stresses dominate ϵ, and thermal gradients are negligible with respect to both ϵ and the surface X-ray flux; i.e. we assume uniform surface temperature ($\delta T = 0$). Then the instantaneous and phase-averaged cyclotron spectra are affected by the distorted magnetic field (i.e. $E_{\rm cyc}$, F, and D depend on M_a; see Section 5). As ϵ also depends on M_a, there are correlations between $E_{\rm cyc}$, F, D, and ϵ.

(d) As for (c), but the magnetic pressure modifies the temperature profile and hence the spectrum via equation (14), without modifying ϵ significantly.

For thermally dominated mountains [scenarios (a) and (b)], we set $\delta T_{lm} \leqslant 0.1$ (Ushomirsky et al. 2000), and assume that δT at the surface equals δT in the crust (i.e. the heat flux is radial). As the solutions in Ushomirsky et al. (2000) do not depend on m, we specialize here to $m = 0$ for convenience, matching the assumption of axisymmetry in $\mathbf{B}$.

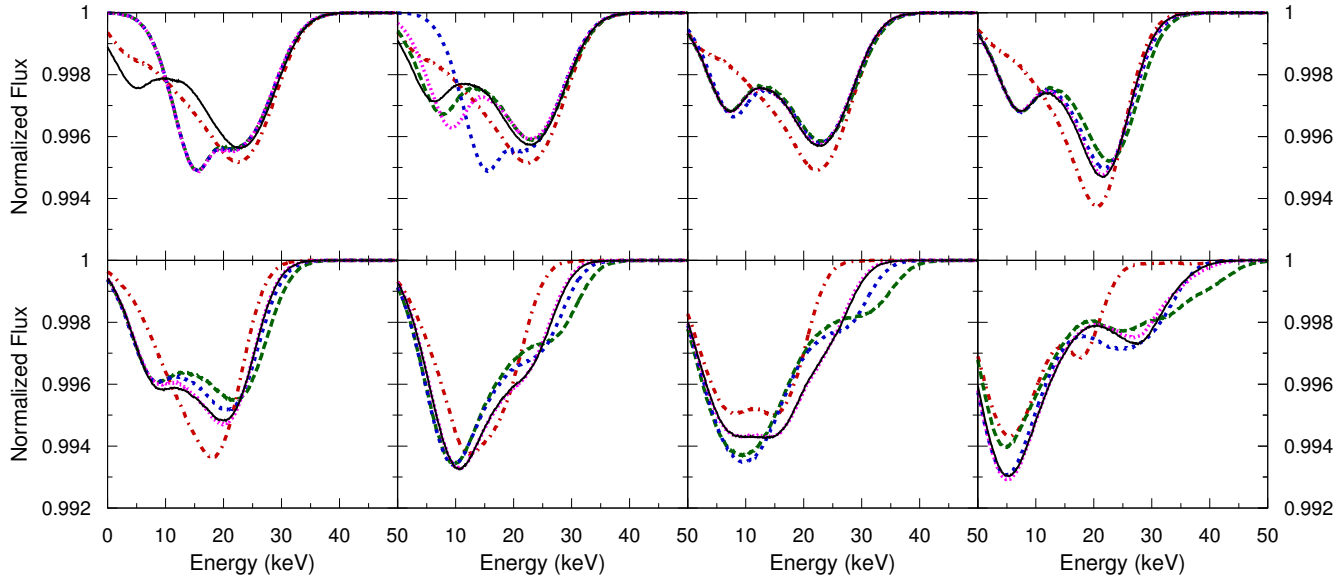

Figure 8. CRSF spectra for a magnetic mountain in the aligned configuration $(\iota, \alpha) = (0, 0)$ (i.e. no phase dependence), with $u = 0.4$, $\psi_* = 10^{24}$ G cm^2, and $M_a/M_c = 10^{-4}$, 10^{-3}, 10^{-2}, 10^{-1} (top row, left to right column), and $M_a/M_c = 0.25$, 0.5, 0.75, 1.0 (bottom row, left to right column). Each panel displays curves corresponding to EOS models A (dot-dashed red), B (short-dashed blue), C (dotted purple), D (long-dashed green), and E (solid black) (Priymak et al. 2011).

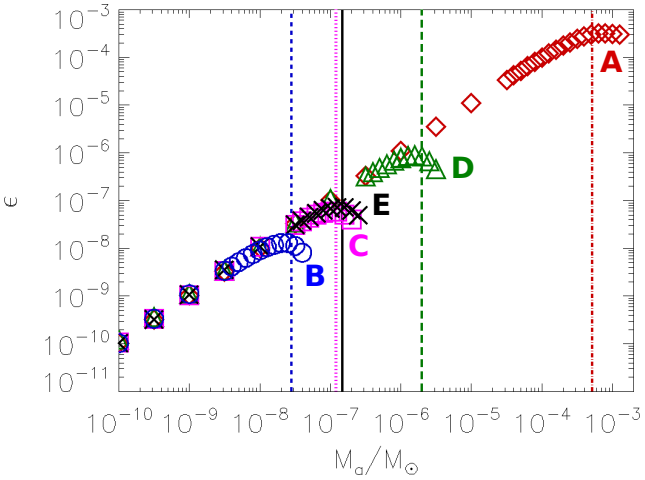

Figure 9. Mass ellipticity ϵ, as a function of accreted mass, M_a, measured in solar masses, for models A (red diamonds), B (blue circles), C (purple squares), D (green triangles), and E (black crosses) [from Priymak et al. (2011)]. Values of the characteristic mass M_c for each model are drawn as vertical dot-dashed/short-dashed/dotted/long-dashed/solid lines and colour-coded accordingly.

For the preliminary study below, we specialize to the orientation $(\iota, \alpha) = (\pi/4, \pi/4)$ for which the line parameters of the phase-resolved spectra from magnetic and thermal mountains vary the most over one period (see Fig. 6), as the LOS crosses the magnetic pole ($\hat{\mathbf{n}}_o \cdot \mathbf{M} = 1$) and equator ($\hat{\mathbf{n}}_o \cdot \mathbf{M} = 0$) at $\omega = \pi/2$ and $\omega = 3\pi/2$ respectively. The EOS in model E of Priymak et al. (2011) is used throughout.

7.2 CRSF signatures

Let us begin by comparing the spectra for the 'hot spot' ($\delta T \propto Y_{10}$) and quadrupole ($\delta T \propto Y_{20}$) models in scenarios (a) and (b). Fig. 10 displays the instantaneous (left panel, $\omega = 3\pi/2$) and phase-averaged (right panel) spectra emitted by a thermal mountain [scenario (a)] for $\psi_* = 1.6 \times 10^{24}$ G cm^2 (black curves), $\psi_* = 1.6 \times 10^{20}$ G cm^2 (red curves), $(\delta T_{10}, \delta T_{20}) = (0.1, 0)$ (dotted curves), and $(\delta T_{10}, \delta T_{20}) = (0, 0.1)$ (solid curves). The left panel exhibits two troughs at $E_{\rm cyc,1} \approx 15$ keV and $E_{\rm cyc,2} \approx 23$ keV. The former is marginally deeper than the latter for $\delta T_{10} \neq 0$ and vice versa for $\delta T_{20} \neq 0$, while the line widths are the same. The right panel exhibits a single absorption feature at ≈ 18 keV for $\delta T_{10} \neq 0$ and ≈ 23 keV for $\delta T_{20} \neq 0$. The pole dominates in the latter case. In comparison, for $\delta T_{10} \neq 0$, the flux-dominating region shifts equatorward, where $|\mathbf{B}|$ is weaker. The instantaneous spectrum exhibits two troughs in

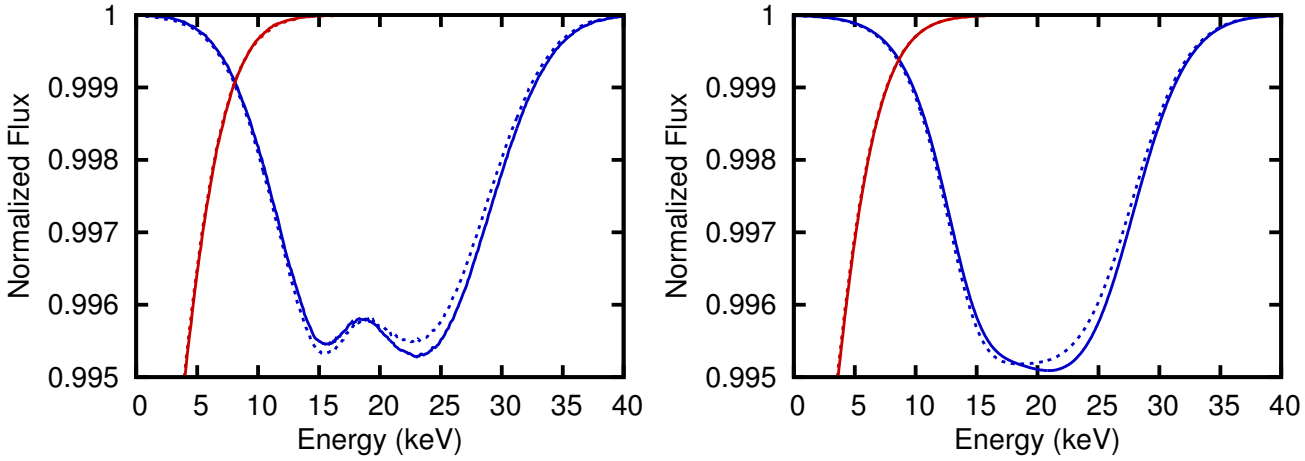

Figure 10. Instantaneous ($\omega = 3\pi/2$, left panel) and phase-averaged (right panel) cyclotron spectrum for scenario (a) (thermal mountain without magnetic burial) with $(\iota, \alpha) = (\pi/4, \pi/4)$ and $u = 0.4$. The results for strong and weak magnetic fields, and 'hot spot' and quadrupole surface temperature distributions, are colour-coded as follows: $\psi_* = 1.6 \times 10^{24}$ G cm^2 (blue curves), $\psi_* = 1.6 \times 10^{20}$ G cm^2 (red curves), $(\delta T_{10}, \delta T_{20}) = (0.1, 0)$ (dotted curves), and $(\delta T_{10}, \delta T_{20}) = (0, 0.1)$ (solid curves).

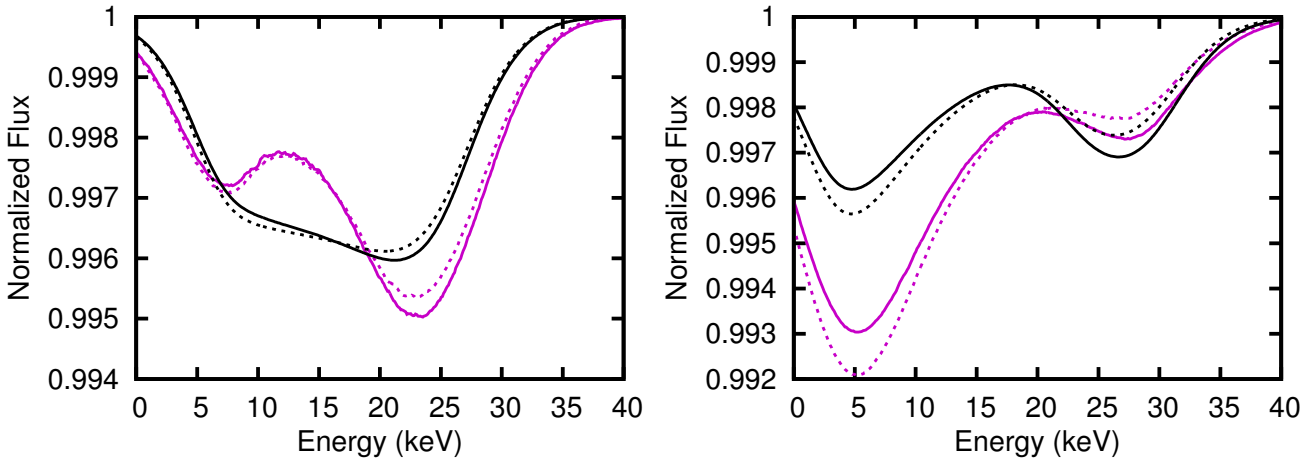

Figure 11. (*Left panel*) Instantaneous ($\omega = 3\pi/2$, purple curves) and phase-averaged (black curves) spectra for scenario (b) (thermal mountain with magnetic burial) with $\psi_* = 1.6 \times 10^{24}$ G cm^2, $(\delta T_{10}, \delta T_{20}) = (0.1, 0)$ (dotted curves), and $(\delta T_{10}, \delta T_{20}) = (0, 0.1)$ (solid curves). Other parameters as for Fig. 10. (*Right panel*) Same as left panel, but for scenarios (c) (solid curves) and (d) (dotted curves) (magnetic mountain with uniform and magnetically modified surface temperature profile respectively).

the narrow window $1.3 \lesssim \omega/\pi \lesssim 1.7$ and one trough elsewhere, so the single trough dominates the phase average.

At low magnetization, e.g. $\psi_* = 1.6 \times 10^{20}$ G cm^2 (red curves in Fig. 10), a single CRSF appears at $\lesssim 5$ keV in both the instantaneous and phase-averaged spectra, with $D \approx 0.99$ and $F \approx 4$ keV. This feature is likely to be interpreted as the non-CRSF continuum in observational data. Note that at low ψ_* ($B/B_{\rm crit} \ll 10^{-2}$) our calculations lie outside the regime of validity of the scattering cross-section formulas in Schönherr et al. (2007). A correct treatment falls outside the scope of this paper.

How does magnetic burial of the sort described in Section 2 affect the CRSF from a predominantly thermal mountain? The left panel of Fig. 11 displays instantaneous ($\omega = 3\pi/2$, purple curves) and phase-averaged (black curves) spectra for scenario (b) with $\psi_* = 1.6 \times 10^{24}$ G cm^2, $(\delta T_{10}, \delta T_{20}) = (0.1, 0)$ (dotted curves), and $(\delta T_{10}, \delta T_{20}) = (0, 0.1)$ (solid curves). Compared to the right panel of Figure 10, the single CRSF in the phase-averaged spectrum is wider ($F \approx 23$ keV) and shallower ($D \approx 0.996$), especially for $\delta T_{10} \neq 0$, to the point where the feature at $E_{\rm cyc} \approx 22$ keV is ill-defined. In the instantaneous spectrum, magnetic burial increases the energy splitting ($E_{\rm cyc,1} \approx 8$ keV, $E_{\rm cyc,2} \approx 23$ keV). The δT_{10} perturbation deepens and suppresses the feature at $E_{\rm cyc,1}$ more than $E_{\rm cyc,2}$, because burial compresses the magnetic field (compare $E_{\rm cyc,1}$ and $E_{\rm cyc,2}$ in the left panels of Figs. 10 and 11).

In scenarios (c) and (d), magnetic burial dominates ϵ and also modifies the cyclotron spectrum. The surface temperature is uniform or magnetic-pressure-corrected respectively. The right panel of Fig. 11 displays the instantaneous ($\omega = 3\pi/2$, purple curves) and phase-averaged (black curves) spectra for scenarios (c) (solid curves) and (d) (dotted curves). Both exhibit CRSFs at $E_{\rm cyc,1} \approx 5$ keV and $E_{\rm cyc,2} \approx 27$ keV. Magnetic pressure support suppresses

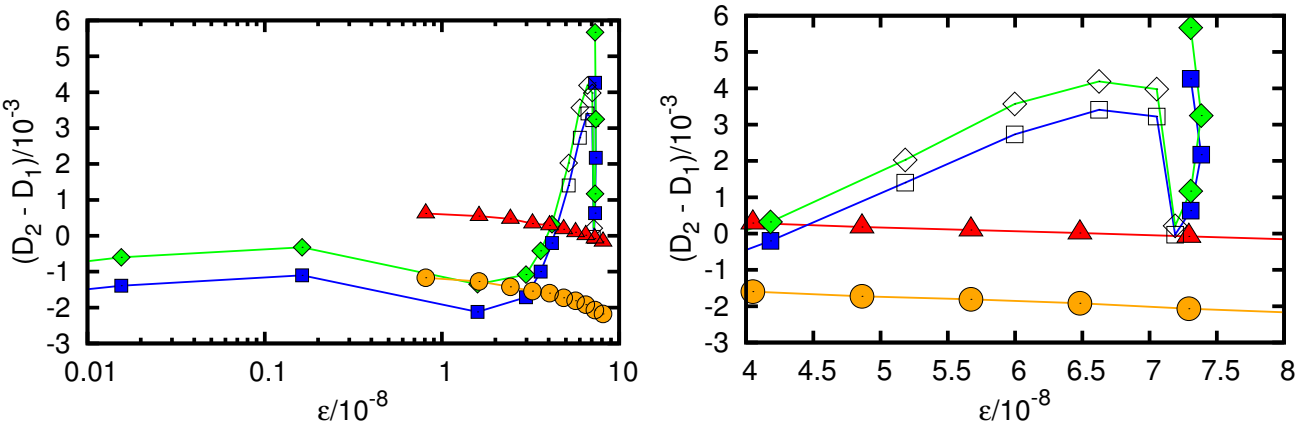

Figure 12. Depth difference $D_2 - D_1$ between the CRSF troughs at $E_{\rm cyc,2}$ and $E_{\rm cyc,1}$ (in normalized flux units) versus mass ellipticity for four different thermally and magnetically dominated mountain scenarios: (a) with $\delta T = \delta T_{20}$ (red curve), (b) with $\delta T = \delta T_{20}$ (orange curve), (c) (blue curve), and (d) (purple curve). The right panel is the same as the left panel but zooms into the region $4 \leqslant \epsilon/10^{-8} \leqslant 8$ for clarity. In the thermal mountain scenarios (a) and (b), $\epsilon(\delta T_{20})$ and $D_2(\delta T_{20}) - D_1(\delta T_{20})$ are computed for $0.01 \leqslant \delta T_{20} \leqslant 0.1$ (red triangles and orange circles respectively, left to right). In the magnetic mountain scenarios (c) and (d), $\epsilon(M_a)$ and $D_2(M_a) - D_1(M_a)$ are computed for $10^{-3} \leqslant M_a/M_c \leqslant 1$ (blue squares and purple diamonds respectively, left to right). Unfilled symbols indicate where the two CRSF troughs merge ($0.4 \lesssim M_a/M_c \lesssim 0.8$) and it becomes difficult to read off $D_2 - D_1$. In all cases, the instantaneous spectrum at $\omega = 3\pi/2$ is used to illustrate the trends.

$E_{\rm cyc,2}$ and deepens $E_{\rm cyc,1}$ (see Section 5), but the magnitude of the effect is modest.

7.3 Ellipticity

The ellipticity ϵ of an accretion mound can be related to its CRSF properties through M_a, if the mountain is magnetically dominated, or δT_{20}, if it is thermally dominated. Future gravitational wave detections of certain classes of accreting neutron stars potentially offer a way to probe this relation and shed new light on accretion mound structure. In scenarios (a) and (b), for $\delta T_{20} \neq 0$, we can write (Ushomirsky et al. 2000)

$$\epsilon \approx 8.1 \times 10^{-7} (R_*/10^6 \text{ cm})^2 (M_*/1.4\ M_\odot)^{-1} \times (T_0/10^8 \text{ K}) (Q/50 \text{ MeV})^3 \delta T_{20}, \quad (15)$$

where Q is the threshold energy for a single electron capture layer, neglecting sinking and shear. In scenarios (c) and (d), we have $\epsilon \approx (M_a/M_\odot)(1 - M_a/M_c)^{-1}$ and M_c given by equation (7). The properties of the CRSF also depend on δT_{20} and M_a, as described in Section 7.2.

Figure 12 plots the depth difference $D_2 - D_1$ between the lines at $E_{\rm cyc,2}$ and $E_{\rm cyc,1}$ in the instantaneous ($\omega = 3\pi/2$) spectrum for scenarios (a) with $\delta T = \delta T_{20}$ (red curve), (b) with $\delta T = \delta T_{20}$ (orange curve), (c) (blue curve), and (d) (purple curve). In the thermal mountain scenarios (a) and (b), $\epsilon(\delta T_{20})$ and $D_2(\delta T_{20}) - D_1(\delta T_{20})$ are computed from equation (15) for $0.01 \leqslant \delta T_{20} \leqslant 0.1$ (in 0.01 increments; red triangles and orange circles respectively, left to right). In the magnetic mountain scenarios (c) and (d), $\epsilon(M_a)$ and $D_2(M_a) - D_1(M_a)$ are computed directly from the output of the GS solver (see Section 2) for $10^{-3} \leqslant M_a/M_c \leqslant 1$ (blue squares and purple diamonds respectively, left to right). Unfilled symbols indicate where two CRSF troughs merge ($0.4 \lesssim M_a/M_c \lesssim 0.8$) and it becomes difficult to read off $D_2 - D_1$; one of the minima effectively becomes a point of inflexion (see Section 5).

Even a small amound of accretion ($M_a = 10^{-2} M_c$) onto a thermal mountain buries the magnetic field sufficiently to decrease $D_2 - D_1$ (orange curve and circles in Fig. 12); cf. scenario (a) (red curve and triangles). Similarly, magnetically modifying the surface temperature through (14) produces an offset in $D_2 - D_1$ compared to the case $\delta T = 0$ in scenarios (c) and (d). In scenarios (a) and (b), the trend in $D_2 - D_1$ versus ϵ is monotonic and unaffected by magnetic burial, unlike in scenarios (c) and (d), where $D_2 - D_1$ behaves nontrivially. Realistically, we expect magnetic and thermal mountains to co-exist in accreting neutron stars, leading to a combination of scenarios (a)–(d). We postpone a more thorough analysis of these trends, including their dependence on orientation, to future work.

7.4 Future observational targets

The accreting neutron stars which are expected to be the strongest emitters of gravitational radiation are LMXBs which possess spin periods $\gtrsim 0.1$ kHz and weak dipole magnetic fields $\lesssim 10^9$ G assuming magnetocentrifugal equilibrium (Ghosh & Lamb 1979). In contrast, objects which show evidence of CRSFs in existing data possess rotation periods of $10^0 - 10^2$ s and magnetic fields of $\sim 10^{12}$ G (inferred from the CRSF line energy). Most CRSFs are in HMXBs with O- and B-type companions, but there are two notable exceptions — Her X−1 and 4U 1626−67 — which are LMXBs. It is commonly thought that the absence of cyclotron features in rapid rotators is explained by their weak magnetization, but an alternative scenario is also possible (see Section 1). A locally compressed, high-order-multipole magnetic field (much stronger than the global dipole) can create a relatively large, gravitational-wave-emitting quadrupole ($\epsilon \lesssim 10^{-7}$) while producing CRSFs which are too weak to be detected by existing X-ray telescopes but may lie within reach of future instruments, as computed in Figures 10 and 11. This 'magnetic fence' scenario (see also Section

1) is supported by evidence that nuclear burning in weakly-magnetized systems is localized by compressed magnetic fields (Bhattacharyya & Strohmayer 2006; Misanovic et al. 2010; Cavecchi et al. 2011; Chakraborty & Bhattacharyya 2012). Combined GS and CRSF calculations indicate that CRSFs with line depths $\gtrsim 0.1\%$ can be obtained for $M_a \lesssim M_c$ and dipole magnetic fields as low as $\sim 10^{11}$ G (Haskell et al. 2014).

We remind the reader that the CRSFs computed here are too weak to be detected by instruments currently in operation, and that the computed ellipticities probably require next-generation gravitational wave detectors like the Einstein Telescope to be detected (Haskell et al. 2014). Several planned X-ray missions are being designed to perform rotation-resolved spectroscopy of the thermal and non-thermal emission from neutron stars in the 0.1–10 keV band. The Neutron star Interior Composition Explorer (NICER) will target precise analysis of X-ray flux modulation due to rotating hot spots and absorption features near ~ 1 keV, achieving $\pm 5\%$ uncertainties in derived quantities (eg. neutron star radius) for a 1 Ms exposure at ~ 10 times the sensitivity of XMM-Newton (Gendreau et al. 2012). This brings light curve modulations at the $\sim 0.3\%$ level predicted by the theory (e.g. see Figure 6) into closer reach. Likewise, the Large Observatory for X-ray Timing (LOFT) is targeting 0.3 keV spectral resolution at ~ 6 keV and is planned to be sensitive to light curve modulations down to an amplitude of $\sim 0.4\%$ for a 100 mCrab source (Feroci et al. 2012).

8 CONCLUSION

In this paper we model the cyclotron spectrum emitted by a magnetically confined accretion mound on an accreting neutron star, extending the pioneering calculations of Mukherjee & Bhattacharya (2012). We calculate the equilibrium hydromagnetic structure of the mound within the GS formalism, including an integral flux-freezing constraint. We model the CRSF as a Gaussian absorption feature, incorporating the emission-angle dependence of CRSF properties, gravitational light bending, and different surface temperature distributions characteristic of magnetically and thermally supported mounds. We show that the instantaneous and phase-averaged spectra seen by an observer contain distinctive features, which can be used in principle to discriminate between mountains of magnetic and thermal origin.

Polar magnetic burial influences the spectrum in the following important ways.

(i) Orientation (Section 3.1). If the observer and magnetic inclination angles satisfy $\pi/8 \lesssim \iota, \alpha \lesssim 3\pi/8$, the phase-resolved spectrum transitions broadly between three states within one rotation period. If either angle approaches $\pi/2$, the spectrum transitions between two distinct states. If either angle approaches zero, the spectrum is phase invariant. The constraints on ι and α thereby obtained are potentially useful in gravitational wave applications.

(ii) Accreted mass (Section 5). As M_a increases, the lateral distortion and equatorial compression of the magnetic field modify the spectrum strongly. For $M_a \ll M_c$, the CRSF properties vary with M_a monotonically. For $M_a \gtrsim 0.5M_c$, the trend breaks down; the troughs merge then separate again. This trend is similar for uniform and magnetic-pressure-modified surface temperature distributions. The low- and high-energy components emanate from the pole (low $|\mathbf{B}|$) and equator (high $|\mathbf{B}|$) respectively.

(iii) EOS (Section 6). Two magnetic mountains with equal M_a and different EOSs exhibit different CRSFs.

CRSFs have been observed in ~ 20 accreting neutron stars, most but not all of which are HMXBs (Pottschmidt et al. 2012; Caballero & Wilms 2012). Generally but not exclusively, it is found that the profile of the fundamental line is asymmetric and not exactly Gaussian, the second harmonic is deeper than the fundamental, the line energy ratio is not harmonic, and there is significant variation of CRSF properties with rotation phase and source luminosity. Other authors have shown that the distorted magnetic field configuration arising from polar magnetic burial can explain some of these observations (Mukherjee & Bhattacharya 2012). We confirm and extend that result here. We also compare the CRSFs produced by thermal and magnetic mountains. Phase-resolved spectra for both kinds of mountains display two troughs at certain phases. After averaging over phase, only one trough remains in a thermal mountain, whereas the magnetic mountain still shows two (Section 7). In systems expected to emit relatively strong gravitational wave signals, perhaps detectable by future instruments like the Einstein Telescope, we show that it is possible in principle to discriminate between mountains of thermal and magnetic origin by correlating X-ray (e.g. line depth difference) and gravitational wave (e.g. wave strain) observables in new multimessenger experiments.

The accretion mound and CRSF models discussed in this paper require further improvements before direct quantitative contact with X-ray and gravitational-wave observations is possible. Time-dependent MHD simulations of thermal transport in mountains are required to address the interaction between the distorted magnetic field and accretion-induced heating, an important source of temperature asymmetries. Extra physics like Hall drift (in the strong-$|\mathbf{B}|$ equator) and Ohmic diffusion (in the polar hot spot) may enter, as well as feedback between the accretion disk and surface mountain, and directional radiative transfer in the accretion column (e.g. the 'fan beam' in subcritical accretors). Also, it is important to extend magnetic mountain simulations to cover the full range of M_a expected in accreting neutron stars (up to $\sim 10^{-1} M_\odot$ in LMXBs). A magnetic mountain loses equilibrium for $M_a \geqslant 1.4M_c$; there is no GS solution available and magnetic bubbles form, which pinch off above $M_a \approx 1.4M_c$ (Payne & Melatos 2004; Mukherjee & Bhattacharya 2012). This behaviour is not the same as a linear or resistive MHD instability (e.g. Parker), which grows from an equilibrium state and possibly disrupts the mountain. Instead, there is no equilibrium state at all (Klimchuk & Sturrock 1989), nor is the mountain disrupted; the bubbles pinch off progressively as M_a increases, keeping the mountain profile near its marginal structure at $M_a \approx 1.4M_c$. This process needs to be studied more. It mainly affects the lower-energy CRSF trough, which is dominated by conditions at the magnetic pole.

We remind the reader that the CRSFs generated from thermal and magnetic mountains are shallow and extremely

challenging to observe with existing X-ray telescopes, especially in the quiescent emission of accreting neutron stars with millisecond spin periods. This paper offers a proof of concept that multimessenger observations with next-generation X-ray and gravitational wave observatories can, in principle, elucidate the surface structure of accreting neutron stars and discriminate between mass quadrupole moments of thermal and magnetic origin.

ACKNOWLEDGEMENTS

The authors thank Brynmor Haskell for comments. This work was supported by a Discovery Project grant from the Australian Research Council.

REFERENCES

Andersson N., Glampedakis K., Haskell B., Watts A. L., 2005, MNRAS, 361, 1153
Araya R. A., Harding A. K., 1999, ApJ, 517, 334
Araya-Góchez R. A., Harding A. K., 2000, ApJ, 544, 1067
Basko M. M., Sunyaev R. A., 1976, MNRAS, 175, 395
Becker P. A., Klochkov D., Schönherr G., Nishimura O., Ferrigno C., Caballero I., Kretschmar P., Wolff M. T., Wilms J., Staubert R., 2012, A&A, 544, A123
Beloborodov A. M., 2002, ApJ, 566, L85
Bhattacharya D., 2012, in 39th COSPAR Scientific Assembly Vol. 39 of COSPAR Meeting, Cyclotron Lines in Accretion Powered Pulsars. p. 172
Bhattacharya D., Mukherjee D., 2011, in Astronomical Society of India Conference Series Vol. 3 of Astronomical Society of India Conference Series, Probing neutron star evolution using cyclotron lines. p. 25
Bhattacharyya S., Strohmayer T. E., 2006, ApJ, 641, L53
Bignami G. F., Caraveo P. A., De Luca A., Mereghetti S., 2003, Nature, 423, 725
Bildsten L., 1998, ApJ, 501, L89+
Brown E. F., Bildsten L., 1998, ApJ, 496, 915
Burnard D. J., Arons J., Klein R. I., 1991, ApJ, 367, 575
Caballero I., et al. 2007, A&A, 465, L21
Caballero I., Wilms J., 2012, Mem. Soc. Astron. Italiana, 83, 230
Cavecchi Y., Patruno A., Haskell B., Watts A. L., Levin Y., Linares M., Altamirano D., Wijnands R., van der Klis M., 2011, ApJ, 740, L8
Chakraborty M., Bhattacharyya S., 2012, MNRAS, 422, 2351
Choudhuri A. R., Konar S., 2002, MNRAS, 332, 933
Chung C. T. Y., Galloway D. K., Melatos A., 2008, MNRAS, 391, 254
Coburn W., Heindl W. A., Rothschild R. E., Gruber D. E., Kreykenbohm I., Wilms J., Kretschmar P., Staubert R., 2002, ApJ, 580, 394
Feroci M., et al. 2012, Experimental Astronomy, 34, 415
Fuerst F., Pottschmidt K., Wilms J., Tomsick J. A., Bachetti M., Boggs S. E., Christensen F. E., Craig W. W., Grefenstette B. W., Hailey C. J., Harrison F., Madsen K. K., Miller J. M., Stern D., Walton D., Zhang W., 2013, arXiv:1311.5514
Gendreau K. C., Arzoumanian Z., Okajima T., 2012, in Society of Photo-Optical Instrumentation Engineers (SPIE) Conference Series Vol. 8443 of Society of Photo-Optical Instrumentation Engineers (SPIE) Conference Series, The Neutron star Interior Composition ExploreR (NICER): an Explorer mission of opportunity for soft x-ray timing spectroscopy
Ghosh P., Lamb F. K., 1979, ApJ, 234, 296
Haberl F., 2007, Ap&SS, 308, 181
Hameury J. M., Bonazzola S., Heyvaerts J., Lasota J. P., 1983, A&A, 128, 369
Harding A. K., 1991, Science, 251, 1033
Harding A. K., Lai D., 2006, Reports on Progress in Physics, 69, 2631
Haskell B., Andersson N., D'Angelo C., Degenaar N., Glampedakis K., Ho W. C. G., Lasky P. D., Melatos A., Oppenoorth M., Patruno A., Priymak M., 2014, ArXiv e-prints
Haskell B., Andersson N., Jones D. I., Samuelsson L., 2007, Physical Review Letters, 99, 231101
Haskell B., Jones D. I., Andersson N., 2006, MNRAS, 373, 1423
Haskell B., Samuelsson L., Glampedakis K., Andersson N., 2008, MNRAS, 385, 531
Heindl W. A., Rothschild R. E., Coburn W., Staubert R., Wilms J., Kreykenbohm I., Kretschmar P., 2004, in Kaaret P., Lamb F. K., Swank J. H., eds, X-ray Timing 2003: Rossi and Beyond Vol. 714 of American Institute of Physics Conference Series, Timing and Spectroscopy of Accreting X-ray Pulsars: the State of Cyclotron Line Studies. pp 323–330
Horowitz C. J., Kadau K., 2009, Physical Review Letters, 102, 191102
Johnson-McDaniel N. K., Owen B. J., 2013, Phys. Rev. D, 88, 044004
Klimchuk J. A., Sturrock P. A., 1989, ApJ, 345, 1034
Klochkov D., Staubert R., Postnov K., Shakura N., Santangelo A., Tsygankov S., Lutovinov A., Kreykenbohm I., Wilms J., 2008, A&A, 482, 907
Kreykenbohm I., Mowlavi N., Produit N., Soldi S., Walter R., Dubath P., Lubiński P., Türler M., Coburn W., Santangelo A., Rothschild R. E., Staubert R., 2005, A&A, 433, L45
Kreykenbohm I., Wilms J., Coburn W., Kuster M., Rothschild R. E., Heindl W. A., Kretschmar P., Staubert R., 2004, A&A, 427, 975
Litwin C., Brown E. F., Rosner R., 2001, ApJ, 553, 788
Makishima K., Mihara T., Nagase F., Tanaka Y., 1999, ApJ, 525, 978
Melatos A., Payne D. J. B., 2005, ApJ, 623, 1044
Melatos A., Phinney E. S., 2001, Publications of the Astronomical Society of Australia, 18, 421
Melatos A., Priymak M., 2013, ApJ, submitted
Meszaros P., 1984, Space Sci. Rev., 38, 325
Mihara T., Makishima K., Nagase F., 2004, ApJ, 610, 390
Misanovic Z., Galloway D. K., Cooper R. L., 2010, ApJ, 718, 947
Mouschovias T. C., 1974, ApJ, 192, 37
Mukherjee D., Bhattacharya D., 2012, MNRAS, 420, 720
Mukherjee D., Bhattacharya D., Mignone A., 2013a, arXiv:1309.0404
Mukherjee D., Bhattacharya D., Mignone A., 2013b, MN-

RAS, 430, 1976
Mukherjee D., Bhattacharya D., Mignone A., 2013c, MNRAS, 435, 718
Mukherjee D., Bhattacharya D., Mignone A., 2013d, arXiv:1304.7262
Nakajima M., Mihara T., Makishima K., Niko H., 2006, ApJ, 646, 1125
Nayyar M., Owen B. J., 2006, Phys. Rev. D, 73, 084001
Nelson R. W., Salpeter E. E., Wasserman I., 1993, ApJ, 418, 874
Nishimura O., 2005, PASJ, 57, 769
Patruno A., Haskell B., D'Angelo C., 2012, ApJ, 746, 9
Payne D. J. B., Melatos A., 2004, MNRAS, 351, 569
Payne D. J. B., Melatos A., 2006, ApJ, 652, 597
Payne D. J. B., Melatos A., 2007, MNRAS, 376, 609
Pfahl E., Rappaport S., Podsiadlowski P., 2003, ApJ, 597, 1036
Piro A. L., Thrane E., 2012, ApJ, 761, 63
Podsiadlowski P., Rappaport S., Pfahl E. D., 2002, ApJ, 565, 1107
Pottschmidt K., et al. 2012, in Petre R., Mitsuda K., Angelini L., eds, American Institute of Physics Conference Series Vol. 1427 of American Institute of Physics Conference Series, A Suzaku view of cyclotron line sources and candidates. pp 60–67
Priest E. R., 1982, Solar magneto-hydrodynamics
Priymak M., Melatos A., Payne D. J. B., 2011, MNRAS, 417, 2696
Riles K., 2013, Progress in Particle and Nuclear Physics, 68, 1
Romanova M. M., Ustyugova G. V., Koldoba A. V., Lovelace R. V. E., 2004, ApJ, 610, 920
Romanova M. M., Ustyugova G. V., Koldoba A. V., Wick J. V., Lovelace R. V. E., 2003, ApJ, 595, 1009
Schönherr G., Wilms J., Kretschmar P., Kreykenbohm I., Santangelo A., Rothschild R. E., Coburn W., Staubert R., 2007, A&A, 472, 353
Spitkovsky A., Levin Y., Ushomirsky G., 2002, ApJ, 566, 1018
Staubert R., Shakura N. I., Postnov K., Wilms J., Rothschild R. E., Coburn W., Rodina L., Klochkov D., 2007, A&A, 465, L25
Suchy S., et al. 2008, ApJ, 675, 1487
Suchy S., et al. 2011, ApJ, 733, 15
Tsygankov S. S., Lutovinov A. A., Serber A. V., 2010, MNRAS, 401, 1628
Ushomirsky G., Cutler C., Bildsten L., 2000, MNRAS, 319, 902
Vigelius M., Melatos A., 2008, MNRAS, 386, 1294
Vigelius M., Melatos A., 2009, MNRAS, 395, 1972
Wang Z., Chakrabarty D., Kaplan D. L., 2006, Nature, 440, 772
Watts A. L., Krishnan B., Bildsten L., Schutz B. F., 2008, MNRAS, 389, 839
Wette K., Vigelius M., Melatos A., 2010, MNRAS, 402, 1099